MONTANA STATE UNIVERSITY

Statistical properties of separators in model active regions

by Brian Thomas Welsch

A thesis submitted in partial fulfillment of the requirements for the degree of Master of Science in Physics
Montana State University
© Copyright by Brian Thomas Welsch (1998)

Abstract:
The magnetic field in the tenuous solar corona is thought to be space-filling, since the ratio of gas pressure to magnetic pressure is much less than unity there (/β = Pgas/Pmagnetic <<1). Observations, however, reveal enhanced X-ray/EUV emission, in the form of "transient brightenings" or "microflares," along only a small subset of field lines. Theoretical considerations suggest that these phenomena should occur along particular topological boundaries in the magnetic field, known as separators. It is along these field lines that magnetic flux is exchanged from one topological domain to another and, as a consequence of this reconnection process, energy is released as the field relaxes to a less complex state. Consequently, knowledge of a field's topological structure allows predictions about the locations and lengths of coronal X-ray/EUV loops in that field configuration.

This topological model is used to study the statistical properties of active region loops. These studies use an active region model described by the interaction of a single element of magnetic flux of one polarity with a much larger distribution of flux of the opposite polarity. The larger distribution of flux is treated in two different ways. In one, it is modelled as a continuous, mean field. In the other, it is that due to many discrete flux elements, whose randomly-chosen locations obey a Gaussian probability distribution function. In this latter case, a Monte Carlo approach was used: statistics were compiled from many realizations of such model active regions to quantify the properties of separators in a way that was insensitive to the details of any one particular distribution. The results obtained by each of these methods are compared, and simple scaling laws for separator lengths are derived. It is shown that separator lengths scale as ~ exp (αr)/√N, where N measures the flux in the large-scale distribution, and r is the distance of the single element from that distribution's center. This scaling law is a theoretical prediction of X-ray loop lengths, which can be compared with observations.

STATISTICAL PROPERTIES OF SEPARATORS IN MODEL ACTIVE REGIONS

by

Brian Thomas Welsch

A thesis submitted in partial fulfillment
of the requirements for the degree

of

Master of Science

in

Physics

MONTANA STATE UNIVERSITY — BOZEMAN
Bozeman, Montana

April 1998

N378
W4649

APPROVAL

of a thesis submitted by

Brian Thomas Welsch

This thesis has been read by each member of the thesis committee, and has been found to be satisfactory regarding content, English usage, format, citations, bibliographic style and consistency, and is ready for submission to the College of Graduate Studies.

Dana W. Longcope, Ph. D. _____ 4/17/98
(Signature) Date

Approved for the Department of Physics

John C. Hermansen, Ph. D. _____ 4-17-98
(Signature) Date

Approved for the College of Graduate Studies

Joseph J. Fedock, Ph. D. _____ 4/24/98
(Signature) Date

STATEMENT OF PERMISSION TO USE

In presenting this thesis in partial fulfillment of the requirements for a master's degree at Montana State University-Bozeman, I agree that the Library shall make it available to borrowers under the rules of the Library.

If I have indicated my intention to copyright this thesis by including a copyright notice page, copying is allowable only for scholarly purposes, consistent with "fair use" as prescribed in the U.S. Copyright Law. Requests for permission for extended quotation from or reproduction of this thesis in whole or in parts may be granted only by the copyright holder.

Signature Brian Welsch

Date 4/17/98

TABLE OF CONTENTS

1. Introduction **1**

How is the Corona Heated? 1

Magnetic Charge Topology 2

2. The Separator Model **7**

A Single Charge in a Background Field 7

Properties of Null Points 9

Intersection of Separatrix with Photosphere 11

A Bipole in a Uniform Field 14

Reconnection Along a Separator 15

3. Active Regions Modeled with Continuous Fields **18**

Continuous Field Limit 19

Methods 20

Probabilistic Arguments 22

Results 30

4. Active Regions Composed of Discrete Flux Elements **36**

Methods 36

Results 41

5. Discussion **46**

Appendices 51

A. A One-Sided Delta Function 52

B. Analytic Expressions for B_r and B_z 53

C. B_r Far from the Origin 57

References Cited 58

LIST OF FIGURES

1 Active Region Images, from SXT & Kitt Peak 3
2 Schematic of Method Used to Find Null, in 1-D 7
3 3-D Separatrix of Charge in a Uniform Background Field 8
4 Cross Section of a Charge's Separatrix in a Uniform Field 13
5 Bipole in a Uniform Background Field 15
6 An Illustration of C_Σ in the Continuous Field Case 23
7 $Q_{enc}(R)$ Integrated in Annular Rings 24
8 $Q_{enc}(R)$ vs. R and $\tilde{P}(R)$ vs. R 26
9 $dQ_{\rm enc}(R)/dR$ vs. R and $d\tilde{P}(R)/dR$ vs. R 26
10 $\langle R \rangle$ and ΔR vs. R 27
11 Comparison of $\langle R_{AB} \rangle$ and $\langle R \rangle$ 29
12 $\langle \ell \rangle$ and $\Delta \ell$ vs. $r_{\rm test}$, in a Continuous Field 31
13 An Exponential Fit to $\langle R \rangle$ vs. $r_{\rm test}$ 32
14 $\langle \ell \rangle$ and $\Delta \ell$ vs. N, in a Continuous Field 33
15 "Opening Angle" of C_Σ vs. N 34
16 C_Σ in a Typical "Footprint" 37
17 Photospheric Field Lines in a Typical Footprint 39
18 Separators in a Typical Footprint 42
19 $\langle \ell \rangle$ vs. $r_{\rm test}$, in a Discrete Field 43
20 $\langle \ell \rangle$ vs. N, in a Discrete Field 44
21 Comparison of $\langle \ell \rangle$ vs. $r_{\rm test}$ Found by Two Methods 46
22 Comparison of $\langle \ell \rangle$ vs. N Found by Two Methods 47
23 Scatter Plot of Charge and Null Separations 49
24 Comparison of Test & Field Charge Separation Distributions Found by Two Methods 50

ABSTRACT

The magnetic field in the tenuous solar corona is thought to be space-filling, since the ratio of gas pressure to magnetic pressure is much less than unity there ($\beta \equiv P_{gas}/P_{magnetic} \ll 1$). Observations, however, reveal enhanced X-ray/EUV emission, in the form of "transient brightenings" or "microflares," along only a small subset of field lines. Theoretical considerations suggest that these phenomena should occur along particular topological boundaries in the magnetic field, known as separators. It is along these field lines that magnetic flux is exchanged from one topological domain to another and, as a consequence of this reconnection process, energy is released as the field relaxes to a less complex state. Consequently, knowledge of a field's topological structure allows predictions about the locations and lengths of coronal X-ray/EUV loops in that field configuration.

This topological model is used to study the statistical properties of active region loops. These studies use an active region model described by the interaction of a single element of magnetic flux of one polarity with a much larger distribution of flux of the opposite polarity. The larger distribution of flux is treated in two different ways. In one, it is modelled as a continuous, mean field. In the other, it is that due to many discrete flux elements, whose randomly-chosen locations obey a Gaussian probability distribution function. In this latter case, a Monte Carlo approach was used: statistics were compiled from many realizations of such model active regions to quantify the properties of separators in a way that was insensitive to the details of any one particular distribution. The results obtained by each of these methods are compared, and simple scaling laws for separator lengths are derived. It is shown that separator lengths scale as $\sim \exp(\alpha r)/\sqrt{N}$, where N measures the flux in the large-scale distribution, and r is the distance of the single element from that distribution's center. This scaling law is a theoretical prediction of X-ray loop lengths, which can be compared with observations.

CHAPTER 1

INTRODUCTION

HOW IS THE CORONA HEATED?

Physicists still do not understand how the solar corona is heated to a temperature of several million kelvins (MK), while the chromosphere, immediately beneath it, is two orders of magnitude cooler. One of two mechanisms is generally held to be responsible. In one view, magnetoacoustic or Alfvén waves (Osterbrock 1961), carry energy from the convection zone, through the chromosphere, and deposit it in the corona. Heating models employing waves, however, face serious difficulties, most notably the "disinclination" of Alfvén waves to deposit energy in the corona (Parker 1988 ; Porter, Klimchuk, & Sturrock, 1994).

In the other view of coronal heating, energy is dissipated directly in the corona as a by-product of some process involving the reconnection of magnetic field lines. At present, however, no known mechanism would allow reconnection to occur in the highly conductive corona. Nonetheless, detailed observations in X-ray (Lin et al. 1984), Hα (Canfield & Metcalf 1987), and simultaneous observations in X-ray and UV (Porter & Klimchuk 1995) have shown that aperiodic events on small spatial scales and short time scales, consistent with reconnection processes, regularly deposit $\sim 10^{27}$ ergs of energy in the corona, suggesting that small-scale, flare-like events might be heating the corona. Since this energy is $\sim 10^{-6}$ that typically seen flares, the term "microflares" has been associated with these phenomema.

Short-term heating of X-ray loops, in the form of "transient brightenings," are also regularly seen in images taken with the soft X-ray telescope (SXT) on board the Yohkoh satellite (Shimizu et al. 1992). These events typically last for a few minutes, and occur with frequencies ranging from one every few minutes to one per hour, depending on just how "active" the host active region is (Shimizu et al. 1992).

Such events are typified by an initial brightening of loop footpoints that leads to brightening of the entire loop, and simultaneous brightenings in multiple loops are not uncommon. For these reasons, Shimizu (1994) attributes these phenomena to "the magnetic interaction of multiple loops."

The fact that estimates of the energy released in these events, $10^{25} - 10^{29}$ ergs (Shimizu 1995), are near estimates of the energy released in microflares (Porter & Klimchuk 1995) has led some (Gary, Hartl, & Shimizu 1997) to speculate that these two flare-like phenomena are, in fact, identical.

Nomenclature aside, these events contribute significantly to coronal heating above active regions. While Porter (1995) argues only that microflares "cannot be dismissed" as a component of active region heating processes, Shimizu (1995) has placed an upper bound on the total energetic contribution of transient brightenings to active region heating at about 20 % of that required to account fully for active region temperatures.

One puzzling aspect of these phenomena is that the mechanism responsible for the brightenings is quite selective. Because the gas pressure in the tenuous corona is much less than the pressure due to the magnetic field there ($P_{\rm gas}/P_{\rm magnetic} \equiv \beta \ll 1$), the magnetic field is believed to fill the entire coronal volume. But the coronal plasma is bright in X-rays along only a few of the field lines above an ordinary active region, as may be seen in the example shown in Figure 1.

Magnetic Charge Topology

Where does the energy that is released in these transient brightenings and microflares originate? The structure of the coronal magnetic field is primarily a product of the distribution of the field at the photosphere. Flux elements seen in magnetograms are interpreted as the cross sections of slender flux tubes whose tops have emerged into the corona (Parker 1955; D'Silva & Choudhuri 1993; Fan, Fisher & McClymont 1994; Caligari, Moreno-Insertis, & Schüssler 1995). Models suggest (Gabriel 1976) that, in the low β plasma above the photosphere, the isolated flux tubes expand to fill space. In the accepted view of flare energetics, photospheric plasma flows

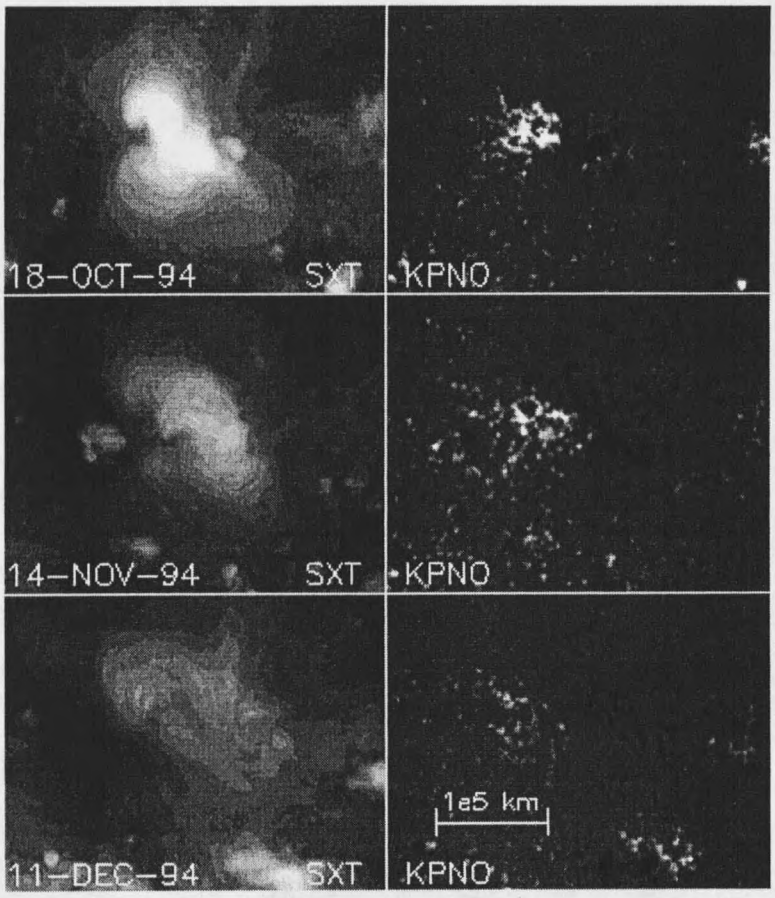


Figure 1: Yohkoh SXT images of an active region, juxtaposed with Kitt Peak line-of-sight magnetograms of the same active region, over three successive solar rotations. (This active region was assigned NOAA AR # 7790 on its first pass). Because the gas pressure is so slight in the tenuous corona ($P_{\rm gas}/P_{\rm magnetic} \equiv \beta \ll 1$), magnetic fields above the active region fill all space. Obviously, however, only a few field lines are bright in soft X-rays. Why? (Courtesy Loren Acton.)

shuffle the locations of these magnetic flux elements. This increases the complexity of the coronal field, gradually increasing the stress, and, hence, the energy stored in that field (Gold & Hoyle 1960; VanHoven et al. 1980). When this energy is suddenly released into the corona, we observe its signature in various ways, most notably in enhanced coronal emission.

The energy release in microflares, like that in "true" flares, is impulsive (Porter & Klimchuk 1995). Further, in both cases, particles are accelerated with sufficient energy to generate X-rays characteristic of $T \sim 10$ MK plasmas. These qualitative similarities suggest that microflares are indeed members of the "flare family" (Porter & Klimchuk 1995). We therefore assume that energy released in microflares and transient brightenings was stored in field stresses before these events.

Since the build-up of stress in the field is typically a rather slow process, the long time scales and small electric fields involved mean the approximations of ideal magnetohydrodynamics (MHD) apply (Longcope 1996). Due to the complexity of coronal fields, theoretical models must include further idealizations to simplify the process of energy storage and release. One approach is to consider simple footpoint distributions (e.g., Hood & Priest 1979) or those exhibiting a high degree of symmetry (e.g., Low 1977).

Another approach, adopted here, involves two assumptions. The first assumption is that the coronal magnetic field is current-free,

$$\mathbf{J} = \nabla \times \mathbf{B} = 0 \quad , \tag{1}$$

meaning it may be represented by the gradient of a scalar potential field,

$$\mathbf{B} = -\nabla\chi \quad . \tag{2}$$

In the second assumption, we take the coronal field to be that which would arise if the flux elements at the photosphere were point-like "magnetic charges,"

$$\mathbf{B} = \sum_{i=0}^{N} \frac{q_i(\mathbf{x} - \mathbf{x'}_i)}{|\mathbf{x} - \mathbf{x'}_i|^3} \quad , \tag{3}$$

where $\Psi_i = 2\pi q_i$ is the flux in footpoint i, and $\mathbf{x}'_\mathbf{i}$ is its location. The field in the corona is then uniquely determined by the solution of Laplace's equation,

$$\nabla \cdot \mathbf{B} = -\nabla^2\chi = 0 \quad , \tag{4}$$

where the distribution of discrete flux elements at the photosphere is imposed as a boundary condition.

By grouping field lines according to their endpoints, classes of field lines are delineated by the various linkages that are possible. In this framework, Sweet (1958) showed that well-defined boundaries exist between basins of differing connectivity, and termed these boundaries *separatrices* and *separators*. Baum & Bratenahl (1980) first quantified the description of the field in topological terms; several authors have since revisited and refined their approach (Gorbachev & Somov 1988; Priest & Forbes 1989; Somov 1992; Lau 1993; Demoulin, Hénoux, & Mandrini 1994; Parnell, Priest, & Golub 1994). Descriptions of magnetic fields in these terms have been grouped under the rubric of *magnetic charge topology* (MCT, Longcope 1996).

These topological boundaries are expected to be the loci of the greatest stresses in the coronal field as photospheric motions rearrange the field's footpoints. Hence, they are the most likely sites of reconnection and consequent energy release, seen in the form of flares and microflares (Longcope 1996). In this context, the selective brightening mechanism revealed in the images in Figure 1 makes sense: field lines near separators emit more energy in the form of X-rays than other field lines because more energy is being deposited there than elsewhere.

In this work, we employ the techniques MCT to make semi-empirical predictions of statistical properties of separators as they would occur in solar active regions. This is the first step in a larger calculation, that of coronal heating rates due to reconnection along separators in active regions. In this work, we calculate the expected length distribution of separator loops occuring in simple models of active regions. These statistical properties can be ascribed to observed coronal X-ray loops. We explore their dependence on quantities one can assign to every active region: size, flux, and number of constituent flux elements.

Shimizu (1994) has compiled statistics on the lengths of coronal loops observed with SXT. As the first step toward an explanation of his results on the basis of theory alone, this investigation is the first theoretical study of its kind. It is also a test of the validity of the MCT model. The work presented here forms the basis of further investigations, already underway, involving more complex models of active regions.

In the next chapter, we describe the separator model in much more qualitative detail, first defining the topological entities to which the model refers, and then briefly discussing energetics in this model. In Chapter 3, we find separator lengths in active regions in which the large-scale fields are approximated by mean fields. In Chapter 4, we find separator lengths in model active regions composed of many flux elements, without averaging. Finally, in the last chapter, we compare and discuss the results obtained with the two different methods.

CHAPTER 2

The Separator Model

A Single Charge in a Background Field

To introduce topological field models, we first consider a single magnetic "test" charge q_B, located at the photospheric surface. We suppose the charge is immersed in a uniform, horizontal background field, which points in what we define to be the $\hat{\mathbf{x}}$ direction, $\mathbf{B} = B_0\hat{\mathbf{x}}$. For concreteness, we suppose the polarity of the test charge is negative, and, further, that it is located at the origin.

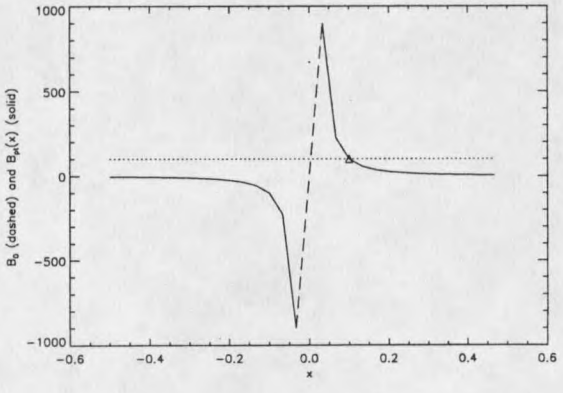


Figure 2: Plots of the constituents of B_x along the $\hat{\mathbf{x}}$ axis: the dotted line is the background field $B_x = B_0$, here given the arbitrary value of 100, while the solid line is $B_x = -(B_{\rm pt}(x,0,0))_x = -q_B/x^2 = +1/x^2$. (The dashed line connects the field of the latter across the field singularity at the charge.) The two curves must intersect at one point; at that point, denoted x_*, the fields cancel, meaning x_* is a *null* point, shown here as a ($\triangle$).

Both the B_y and B_z components of the field vanish identically along the $\hat{\mathbf{x}}$ axis. The remaining component, B_x, vanishes at the point $\mathbf{x}_*$, at which

$$B_0 = \frac{q_B}{|\mathbf{x}_*|^2} = \frac{q_B}{x_*^2} \quad , \tag{5}$$

with $\mathbf{x}_* = (x_*, 0, 0)^T$, where $x_* > 0$ (see figure (2)). The location of the null is then easily seen to occur at

$$x_* = \sqrt{\frac{q_B}{B_0}} \quad . \tag{6}$$

Most field lines in this configuration can be grouped into two categories, according to their endpoints: 1) field lines which start at negative infinity and end at q_B, i.e., those field lines which connect the background field to q_B; and 2) field lines constituting the background field, i.e., those with both endpoints far from the test charge. Field lines which constitute the boundary between these two domains can end

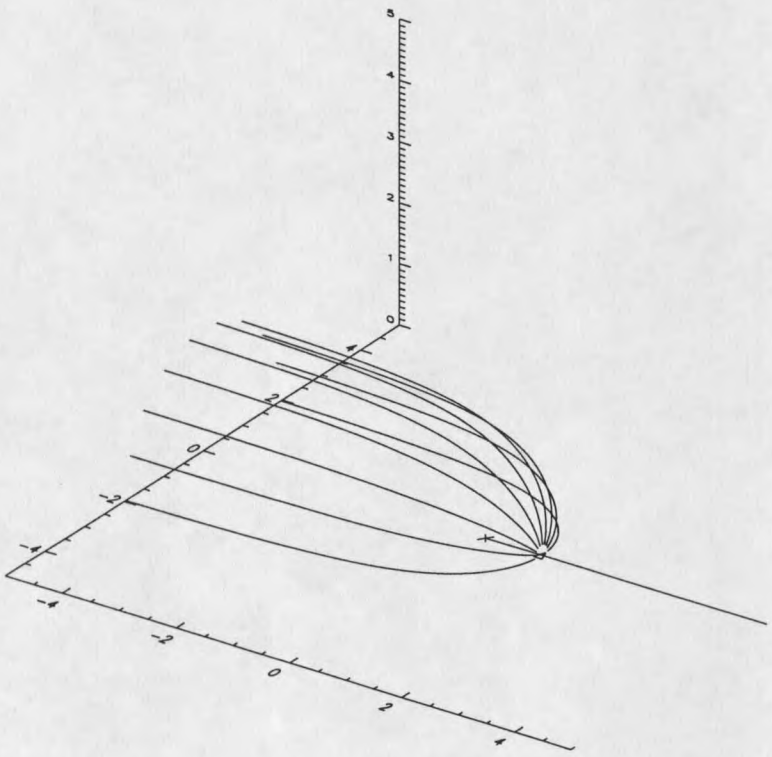


Figure 3: A selection of field lines on test charge's separartrix surface: they begin at $-\infty$, and end at the null at $\mathbf{x}_*(\triangle)$. Collectively, we label all the lines in the surface Σ. All field lines within the separatrix begin at $-\infty$ and end at the test charge, while all those without begin at $-\infty$ and end at $+\infty$. Also shown are the null's γ-lines, the field lines that leave the null: one runs from the null to the test charge, while the other runs to $+\infty$.

at neither q_B nor infinity, and thus fall into a third category: they begin at negative

infinity and end at the location of the null, $\mathbf{x}_*$. These field lines form the test charge's *separatrix surface*, which we label Σ (Figure 3).

Properties of Null Points

Near the null, the magnetic field can be expanded in a Taylor series,

$$\mathbf{B}(\mathbf{x}_* + \Delta\mathbf{x}) = \mathbf{M}(\mathbf{x}_*) \cdot \Delta\mathbf{x} + \cdots \quad , \tag{7}$$

where the elements of the Jacobian matrix $\mathbf{M}(\mathbf{x}_*)$ are $M_{ij} = \frac{\partial B_i}{\partial x_j}|_{x_*}$. Since the field is force-free, the matrix is symmetric and thus has three real eigenvalues, and three orthogonal eigenvectors (Longcope 1996). As $\nabla \cdot \mathbf{B} \equiv 0$, two eigenvalues must differ in sign (Cowley 1973; Yeh 1976), and the sign of the third delineates two classes of nulls (Cowley 1973): a null is A-type if two eigenvalues are negative, and B-type if two are positive.

This delineation of two classes of nulls, based upon the sign of the intermediate eigenvalue of the Jacobian matrix, neglects the possibility that this eigenvalue may vanish. The null in such a case is not *generic*; we digress to discuss briefly this eventuality. Consider a null in some configuration in which the intermediate eigenvalue of the Jacobian though small, is nonzero. By changing the amplitude of a charge near the null, both the null's location and the Jacobian are perturbed. When the intermediate eigenvalue is sufficiently small, such a perturbation can change the sign of the eigenvalue. If so, the null undergoes a pitchfork bifurcation: two nulls of the same type as the original appear, one just above and one just below the photosphere, and another of the opposite type appears in place of the old. These bifurcations are in fact seen in numerical simulations; as the properties of such configurations are beyond the scope of the current theory, however, only generic cases are considered in all that follows.

In general, field lines leave (enter) an A-type (B-type) null along two lines which run in opposite directions along the eigenvector corresponding to the null's sole positive (negative) eigenvalue. These are the null's γ-lines, or "spines" (Parnell, Priest, & Golub 1994) one runs from (to) the null to (from) the charge, while the other is

connected to a charge that gives rise to part of the background field. Clearly, then, an A-type (B-type) null is associated with a negative (positive) charge. Since the null at $\mathbf{x}_*$ is A-type, we rename its location $\mathbf{x}_\mathbf{A}$.

At a microscopic level, very near the null, field lines enter (leave) an A-type (B-type) null in the two-dimensional surface spanned by the two negative (positive) eigenvectors, forming a so-called "fan" (Parnell, Priest, & Golub 1994) in a plane. Further from the null, the macroscopic field deforms the flat plane into a curved surface.

Field lines on a given side of this surface have an endpoint at the same charge that the γ-line on that side of the surface does. This means that the separatrix forms the boundary between field lines having different connectivity. Hence, a given charge's separatrix demarcates the volume which contains all of that charge's flux.

In our example, the eigenvectors corresponding to the negative eigenvalues of $\mathbf{M}$ at A are perpendicular to the $\hat{\mathbf{x}}$-axis, and the separatrix surface is thus locally tangent to a plane parallel to the $y-z$ plane. This tangent plane bisects the $\hat{\mathbf{x}}$-axis at $\mathbf{x}_\mathbf{A}$.

What we have been calling "the background field" must, ultimately, be due to another charge or charges. Hence, we have in fact been considering a configuration of at least two charges. How did we associate "the null" with "the charge"? We digress to consider this question. In a configuration with multiple charges, and only generic nulls, one can argue that the number of nulls is one fewer than the number of charges. The presence of an "orphan" charge notwithstanding, however, it is in principle possible to associate a particular null with each charge, and vice versa. To understand this, imagine that a charge is added to a configuration of charges by being "turned on," in the sense that its amplitude is raised from zero in small steps. The instant the charge appears, a null also appears, quite near the charge, and the two are easily associated merely by their proximity: their separation is given by equation (6). (One can imagine, however, that, as the charge's amplitude is increased further and the null-charge separation increases, the null can move away from the charge in a way that is not easy to predict, due to variations in the background field. Consequently, in practice, it is nontrivial to find the null associated with a particular charge in a

given configuration.)

Intersection of Separatrix with Photosphere

Much of the work presented on the following pages involves the field lines at the intersection of a test charge's separatrix with the photosphere. It is therefore appropriate to derive the equation of this curve, which we label $\mathcal{C}_\Sigma$, in the monopole example now, for comparison to work discussed below. The easiest way to proceed takes advantage of the symmetry of this configuration to represent the fields using Clebsch variables (Moffatt 1978). It is expedient to operate in a cylindrical coordinate system, $(\rho'(x,y,z), \phi'(x,y,z), z'(x,y,z))$, where the following transformations give the new coordinates in terms of the old:

$$\rho' = \sqrt{y^2+z^2} \tag{8}$$

$$\phi' = tan^{-1}\left(\frac{y}{z}\right) \tag{9}$$

$$z' = x \tag{10}$$

In the new coordinates, the field is symmetric about the $\hat{\mathbf{z}}'$-axis, and can be written in terms of a flux function, $f(\rho', z')$:

$$\mathbf{B}(\rho', \phi', z') = \nabla f \times \nabla \phi' = -\frac{1}{\rho'}\hat{\phi}' \times \nabla f \quad , \tag{11}$$

where the gradient is in cylindrical coordinates. The flux function is the sum of contributions from the uniform background field and the point charge,

$$f^{(\mathrm{b})} = -\frac{(\rho')^2}{2}B_0 + f_0^{(\mathrm{b})} \tag{12}$$

$$f^{(\mathrm{pt})} = -\frac{q_B z}{\sqrt{(\rho')^2+(z')^2}} + f_0^{(\mathrm{pt})} \tag{13}$$

$$\Longrightarrow f = -\frac{(\rho')^2}{2}B_0 - \frac{q_B z}{\sqrt{(\rho')^2+(z')^2}} + f_0^{(\mathrm{b})} + f_0^{(\mathrm{pt})} \quad . \tag{14}$$

In what follows, we take the (arbitrary) constants that appear in the equation above, $f_0^{(\mathrm{b})}$ and $f_0^{(\mathrm{pt})}$, to be zero. The advantage of this formulation is that contours of f are field lines. So, to find the equation of the field lines that form $\mathcal{C}_\Sigma$, we evaluate f at

the coordinates of A in the new system, $(0, \sqrt{q_B/B})$,

$$f\Big|_A = f\Big(0, \sqrt{\frac{q_B}{B_0}}\Big) = -q_B \quad , \tag{15}$$

and then solve for $\rho'(z')$, since

$$\frac{q_B z'}{\sqrt{(\rho')^2 + (z')^2}} + \frac{B_0}{2}(\rho')^2 = q_B \tag{16}$$

obtains along this field line. Defining $a \equiv \sqrt{\frac{q_B}{B_0}}$, this can be written

$$\Big(1 - \frac{(\rho')^2}{2a^2}\Big)^2 = \frac{(z')^2}{\rho^2 + (z')^2} \quad , \tag{17}$$

which, after a little algebra, reduces to

$$(\rho')^2\Big[1 - \frac{(\rho')^2}{2a^2}\Big]^2 = (\rho')^2\frac{(z'^2)}{a^2}\Big[1 - \frac{(\rho')^2}{4}\Big] \quad . \tag{18}$$

Because both the null's γ-lines and $\mathcal{C}_\Sigma$ run through the null, f takes the same value on both. Since we want the equation for $\mathcal{C}_\Sigma$, we must factor out the solutions for the γ-lines, which run along the axis ($\rho' = 0$). Doing so leaves a bi-quadratic in $\rho'(z')$,

$$1 - \frac{(\rho')^2}{a^2} + \frac{1}{4}\frac{(\rho'^4)}{a^4} = \frac{(z')^2}{a^2} - \frac{1}{4}\frac{(\rho')^2}{a^2}\frac{(z')^2}{a^2} \quad ,$$

which yields, after application of the quadratic equation,

$$\frac{(\rho')^2}{a^2} = 2\Bigg[\Big(1 - \frac{1}{4}\frac{(z')^2}{a^2}\Big) \pm \sqrt{\frac{1}{2}\frac{(z')^2}{a^2} + \frac{1}{16}\frac{z'^4}{a^4}}\Bigg] \quad . \tag{19}$$

In Figure 4, we have plotted $\rho'(z')$, which is a cross section of the test charge's separatrix surface.

The $(-)$ root gives the correct $\rho'(z')$ for z' on $[0, a]$, while the $(+)$ root yields $\rho'(z')$ on $z = (-\infty, 0)$. When $z' \ll 0$, and $|z'| \gg a$, one can factor $(\frac{z'}{2a})^4$ out of the radical and expand the result in a binomial series, which gives, to order $(\frac{a}{z'})^2$:

$$\frac{(\rho')^2}{a^2} = 2 - \frac{(z')^2}{2a^2} + \frac{(z')^2}{2a^2}\sqrt{1 + \frac{8a^2}{(z')^2}} \tag{20}$$

$$\simeq 2 - \frac{(z')^2}{2a^2} - \frac{(z')^2}{2a^2} + \frac{(z')^2}{2a^2}\Big(\frac{4a^2}{(z')^2}\Big) = 4 \tag{21}$$

$$\Longrightarrow \rho'(\infty) = 2a \tag{22}$$

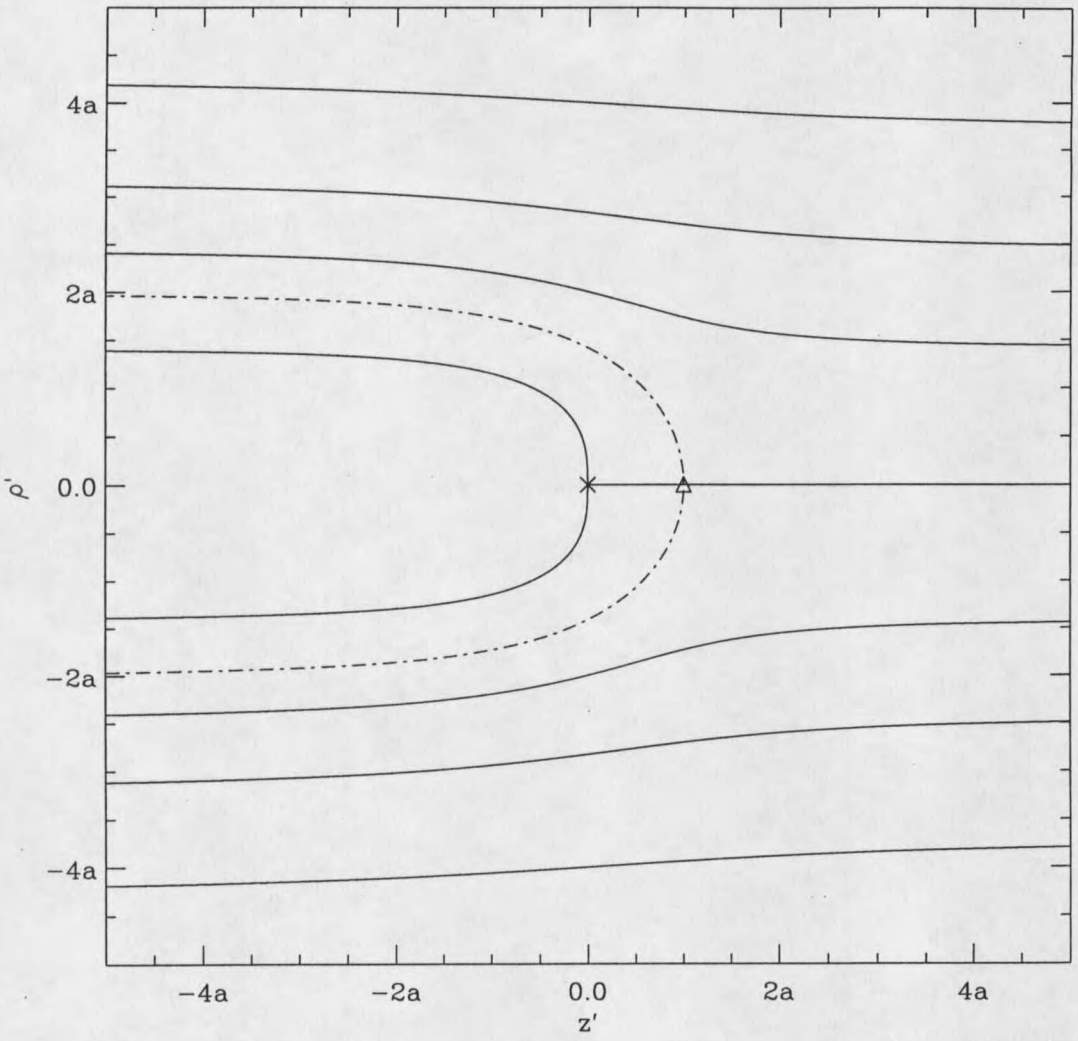


Figure 4: Contours of the flux function f: $f = q_B$ is a cross section of the test charge's separatrix surface (dash-dot) and runs through the null at $x = a = \sqrt{q_B/B_0}$, which is denoted with a ($\triangle$). The null's γ-lines are also shown: one runs from the null to the charge, while the other runs to $+\infty$. The values of f along the other field lines are $8\,q_B, 4\,q_B, 2\,q_B$ (all outside separatrix), and 0.0 (within separatrix). z' runs along the abscissa, while ρ' runs along the ordinate.

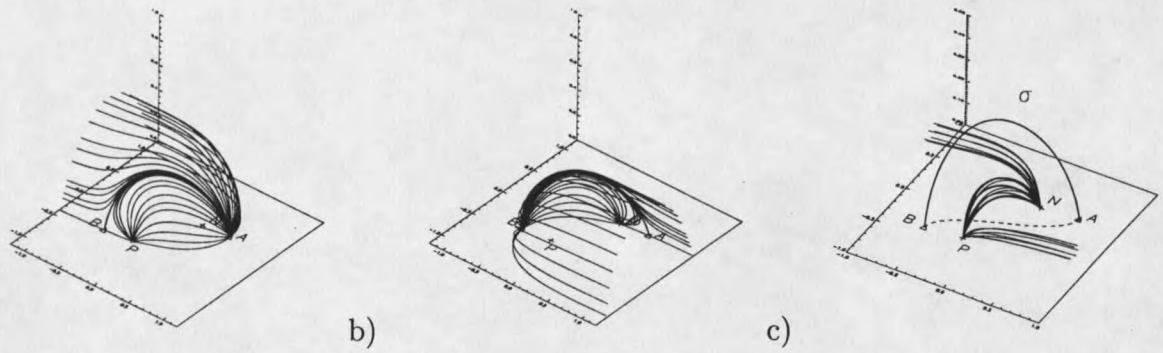
Recalling that, in the the original coordinate system's $z = 0$ plane, ρ' is equivalent to the y direction, we see that the field lines which form the intersection of the test charge's separatrix with the photosphere asymptotically approach two lines parallel to the $\hat{\mathbf{x}}$-axis, at $y = \pm 2a$ above and below it.

A Bipole in a Uniform Field

We now modify the simple configuration described above by placing an additional test charge at the photospheric surface. We suppose that the new charge is located at $\mathbf{x_2}$ with respect to the origin, and has the same magnitude as the original charge, but the opposite sign. The new charge, of course, interacts with the background field: it is also associated with a null, this time of type B, which is located at point B, with $\mathbf{x_B} \simeq \mathbf{x_2} - \sqrt{q_B/B_0}\hat{\mathbf{x}}$; and it has its own separatrix surface, Σ_B which encloses its flux.

If the new charge is "far" from the original one, its separatrix looks very much like the first charge's, but differs in its orientation: it opens away from the background field, i.e., in the $+\hat{\mathbf{x}}$ direction. Far, in this context, means the charges' separation is much greater than the characteristic length $\sqrt{q_B/B_0}$. Because this length approximates the half-width of each charge's separatrix, the two charges' separatrices do not intersect in this case. This means no field lines have endpoints at both charges, or, equivalently, that the two charges do not share flux with each other. In this case, then, the analysis used to describe the field topology in the single-charge case applies equally well to each individual charge.

If, however, the charges are "close" with respect to this same length, then they can share flux with each other, and we denote this shared flux by ψ_{12}. In this case, there are two additional topological categories of field lines. The first class contains those lines which originate at one charge and end at the other; these field lines, from the very definition of a separatrix, lie within that volume enclosed by both of the charges' separatrices. The other class contains only one field line, that formed by the intersection of the two separatrix surfaces. It is called a *separator*, and we label it σ (see Figure 5); it encircles all of those field lines which have endpoints at the two



a) b) c)

Figure 5: a) The separatrix Σ_A encloses the flux N shares with the background field and P. b) The separatrix Σ_B encloses the flux P shares with the background field and N. c) The intersection of Σ_A with Σ_B forms the separator loop, σ. The only field line on both separatrices, it must begin at the B-type null and end at the A-type null. In the last figure, a selection of the bipole's field lines is shown, along with some of the lines that connect each constituent of the bipole to the background field. (Figures taken from Longcope 1998.)

charges, and no others (Longcope & Cowley 1996). Combining a line segment which runs from A to B in the plane at $z = 0$ with the separator σ forms a complete loop, labeled $\mathcal{C}$. The line integral of the magnetic vector potential $\mathbf{A}$ along this loop returns just this shared flux,

$$\psi_{12}^{(\mathrm{v})} = \oint_{\mathcal{C}} \mathbf{A} \cdot \mathbf{dl} \ , \tag{23}$$

where the direction of the integral is such that the integration proceeds parallel to the magnetic field along σ, and the superscript (v) reminds us that this is the vacuum flux (Longcope 1996).

Reconnection Along a Separator

Longcope & Cowley (1996) developed a model to predict how the plasma in the configuration above would react to perturbations, e.g., displacement of the field sources, as might be caused by turbulent flows in the photospheric plasma. An outline of their theory is presented here to illuminate which quantities are pertinent to calculations of coronal heating rates in the separator model.

Any displacement of the two test charges in the example above, in general, affects several of the quantities of interest in the configuration: the location of the nulls

changes, the shape of σ is altered, and the net vacuum flux enclosed by $\mathcal{C}$ changes by an amount $\Delta\psi_{12}^{(\mathrm{v})}$. A change in flux through the surface enclosed by $\mathcal{C}$ induces, by Faraday's Law, an electromotive force (emf) $\mathcal{E}$ along the separator. But the plasma, which we assumed to be a perfect conductor, cannot support a parallel electric field; instead, a *current ribbon* instantaneously forms along the separator, with total current I flowing in such a way as to generate a self-flux $\psi^{(\mathrm{cr})}(I)$, which exactly cancels $\Delta\psi_{12}$ (Longcope & Cowley 1996), viz.,

$$\psi_{12}^{(\mathrm{v})} + \psi^{(\mathrm{cr})}(I) = \psi_0 + \Delta\psi_{12}^{(\mathrm{v})} + \psi^{(\mathrm{cr})}(I) = \psi_0 \quad . \tag{24}$$

Longcope (1996) has parametrized $\psi^{(\mathrm{cr})}$ in terms of the ribbon current I, in the small $|I|$ limit, to be given by

$$\psi^{(\mathrm{cr})} = \frac{\ell I}{c} \ln\left[256 e^{-3} \frac{I^*}{|I|}\right] \quad , \tag{25}$$

where ℓ is the separator length, and I^* is related to the average shear in the vacuum field along the separator. Inverting this equation yields an expression for $I(\psi^{(\mathrm{cr})})$, which can be used to calculate the energy difference between the current-free field and the field with the current ribbon,

$$\Delta\mathcal{E} = \frac{1}{c}\int_0^{\psi^{(\mathrm{cr})}(I)} d\psi\, I(\psi) = \frac{\ell I^2}{2c^2} \ln\left[256 e^{-\frac{7}{2}} \frac{I^*}{|I|}\right] \quad , \tag{26}$$

which is energy due to the self-inductance of a loop in which a current is first turned on and then ramped up to some final value $\psi^{(\mathrm{cr})}$. The salient point for this discussion is that this expression for the energy depends directly upon the current, I, and the separator length, ℓ. The primary goal of this work is to determine the statistical properties of the latter, a purely geometric quantity.

Qualitatively, the separator model can be explained as follows. First and foremost, the coronal field is assumed to be entirely potential, and is therefore in a stable state of minimum energy. Motion of the field lines' footpoints will alter the vacuum flux enclosed by a given separator; this will, in turn, induce current to flow in a ribbon along that separator, such that the net flux through it remains constant. If, via some instability, reconnection then occurs at the separator, flux will be transferred across the separator until the field relaxes to a new potential configuration, and the

current ribbon will disappear. Excess energy due to the ribbon current will then be liberated, heating the coronal plasma and evaporating chromospheric plasma in the neighborhood of the separator. This, in turn, will be seen as sudden X-ray brightening near the separator (Longcope 1998).

CHAPTER 3

Active Regions Modeled with Continuous Fields

Solar active regions are composed of many individual flux elements, which can be modeled as magnetic charges of varying strengths (Longcope 1996). Accordingly, we now generalize to the multiple charge case.

We first consider a large-scale distribution composed of N much smaller flux elements, all of the same flux. The field is given by

$$\mathbf{B}(\mathbf{x}) = \sum_{i=1}^{N} \frac{q_0(\mathbf{x} - \mathbf{x}_\mathbf{i}')}{|\mathbf{x} - \mathbf{x}_\mathbf{i}'|^3} \quad , \tag{27}$$

where $\Psi_0 = 2\pi q_0$ is the flux in each constituent magnetic charge, the $\mathbf{x}_\mathbf{i}' = (x_i', y_i', 0)$ are the locations of these flux elements, and where we have taken the $z = 0$ plane to lie at the photosphere.

Such a configuration is a rudimentary model of an active region of total flux $q_0 N = 10^{21}$Mx, where $q_0 \approx 10^{19}$Mx, and the field in each element is $\approx 1kG$ (Priest 1982), and the number of elements N is on the order of 100. In a typical such active region, the elements would be distributed within an area measuring tens of Mm in diameter (cf., Figure 1). In practice, the coordinate axes are always assumed to be scaled such that the distribution's width, δ, is one.

We assume the magnetic flux elements in a large, initially compact, region of concentrated magnetic flux will diffuse by a random walk, due to turbulent plasma motions at the photosphere (Leighton 1964 ; see also Figure 1). Thus, it is appropriate to model the probability distribution describing the flux elements' locations as Gaussian,

$$p(x_i', y_i') \propto \exp\left(\frac{-[(x_i')^2 + (y_i')^2]}{2\delta^2}\right) \quad , \tag{28}$$

where δ is the width of this distribution, as discussed above.

To create such a distribution, we use a random number generator that returns normally-distributed values, with a mean of zero and a standard deviation of one,

for the various flux elements' coordinates (x_i', y_i'). Since results derived from a single realization of such a model active region are statistically meaningless, we must use results determined from many realizations of such distributions (a Monte Carlo method) to find "ensemble averaged" quantities.

Continuous Field Limit

When N is large, using the expression for the field in equation (27) to find nulls and topologically important field lines is feasible only with numerical methods. We expect, however, that expressions for ensemble-averaged quantities could be more easily attacked with analytic methods. Accordingly, we now consider such averages.

To further simplify our task, we assume that the field topology above the photosphere is delineated by the topology of field lines at the photosphere, meaning we only need to find expressions for the field at $z = 0$. Since the field is potential, the radial field at $z = 0$ is related to the vertical field by Laplace's equation. As we have assumed the functional form of the latter is Gaussian, we begin by deriving an expression for the average vertical magnetic field at the photosphere. The $\hat{\mathbf{z}}$-component of the discrete field (27) there is given exactly by

$$B_z(x, y, 0) = q_0 \lim_{z \to 0} \sum_{i=1}^{N} \frac{z}{[(x - x_i')^2 + (y - y_i')^2 + z^2]^{3/2}} \quad , \tag{29}$$

which is zero except at the charges' locations, $(x, y, 0) = (x_i', y_i', 0)$, where it diverges. Now consider averaging over an infinite number of collections of N pairs of coordinates $\{(x_i', y_i', 0)\}$, i.e., an ensemble of sets of charge locations,

$$\langle B_z(x, y, 0) \rangle = q_0 \sum_{i=1}^{N} \lim_{z \to 0} \langle \frac{z}{[(x - x_i')^2 + (y - y_i')^2 + z^2]^{3/2}} \rangle \tag{30}$$

The average inside the sum can be written explicitly,

$$\lim_{z \to 0} \langle \frac{z}{[(x - x_i')^2 + (y - y_i')^2 + z^2]^{3/2}} \rangle$$

$$= \lim_{z \to 0} \int_{-\infty}^{\infty} dx_i' \int_{-\infty}^{\infty} dy_i' \frac{z\, p_i(x_i', y_i')}{[(x - x_i')^2 + (y - y_i')^2 + z^2]^{3/2}} \quad , \tag{31}$$

where each member $(x_i', y_i', 0)$ of each set $\{(x_i', y_i', 0)\}$ obeys the same probability distribution, specifically, that discussed in the previous section, $p_i(x_i', y_i') \propto \exp(-[x_i'^2 +$

$y_i'^2]/2\delta^2)$. Changing coordinates, $x_i = (x - x_i')$, etc., and defining $r_i = (x_i^2 + y_i^2)^{1/2}$, the integrals for the i^{th} charge become

$$\int \frac{z\, p_i(x_i', y_i') dx_i' dy_i'}{[(x - x_i')^2 + (y - y_i')^2 + z^2]^{3/2}} = \int_0^{2\pi} d\phi \int_0^{\infty} dr_i \left\{ \frac{z\, r_i}{[r_i^2 + z^2]^{3/2}} \right\} p_i(x - x_i, y - y_i) \quad . \tag{32}$$

In Appendix A., we consider the properties of the quantity in curly braces in this equation, a function we label $D(r_i, z)$,

$$D(r_i, z) \equiv \left\{ \frac{z\, r_i}{[r_i^2 + z^2]^{3/2}} \right\} \quad , \tag{33}$$

and show that

$$\lim_{z \to 0} D(r_i, z) = \delta(r_i) \quad . \tag{34}$$

This makes evaluation of the integral in equation (32) trivial,

$$\int_0^{2\pi} d\phi \int_0^{\infty} dr_i \delta(r_i) p_i(x - x_i, y - y_i) = 2\pi p_i(x, y) \tag{35}$$

Since $r_i = 0$ corresponds to $(x_i', y_i') = (x, y)$, the probability distribution we assumed in equation (31) becomes $p_i(x, y) \propto \exp(-[x^2 + y^2]/2\delta^2)$, and we can finally write an expression for $\langle B_z(x, y, 0) \rangle$ in equation (30),

$$\begin{aligned} \langle B_z(x, y, 0) \rangle &= q_0 \sum_{i=1}^{N} \exp\left(-\frac{[x^2 + y^2]}{2\delta^2} \right) && (36) \\ &= 2\pi q_0 N \exp\left(-\frac{[x^2 + y^2]}{2\delta^2} \right) && (37) \\ &= 2\pi q_0 N e^{\frac{-r^2}{2\delta^2}} . && (38) \end{aligned}$$

Hence, the average vertical field, like probability distribution of each set of charge locations, is Gaussian. In the following discussion, we shall use $\overline{B}_z$ to mean $\langle B_z(x, y, 0) \rangle$.

METHODS

Now that we have a much more tractable form for the vertical field in our expression for $\overline{B}$, some headway can be made using analytical methods. As above, we consider one "test" charge, this time immersed in the non-uniform background field

arising from a collection of "field" charges. For a separator to exist, the test charge must share flux with the background field, which means its sign must be opposite that of the background field.

The primary result sought is the probability distribution of separator lengths, as a function of both the location of the test charge, and the test charge's strength. We proceed under two assumptions: 1) the probability that a separator connects the test charge's null with a field charge's null is directly related to the probability that the test charge shares flux with a field charge, and 2) the probability that the test charge shares flux with a field charge is an increasing function of the amount of vertical flux $\overline{B}_z$ contained within the closed curve $\mathcal{C}_\Sigma$ (the intersection of the test charge's separatrix with the photosphere). We adopt the first assumption because the existence of separatrices is a necessary condition for the existence of a separator. We embrace the second because the average vertical field's distribution is identical to the field charges' spatial probability distribution; hence, "more vertical field enclosed" equates to "more probability of enclosing a field charge."

Our first task must therefore be to find the two field lines that form $\mathcal{C}_\Sigma$. Superposing the field of a test charge, also located at the photosphere, but some distance away from the background field's centroid, breaks the azimuthal symmetry of the combined field. For this reason, the approach using Clebsch variables employed before cannot be used now. Instead, we must find the radial field at the photosphere, and then integrate the field line equation from the test charge's null. (Recall that every field line in Σ_{test} has a terminus here.) To take advantage of the combined field's remaining "mirror" symmetry, we place the origin at the background field's centroid, and align the $\hat{\mathbf{x}}$-axis with the line from the origin to the test charge's location, which makes the latter quantity $\mathbf{x_0} = (x_0, 0, 0)^T$.

The contribution of the background field to the total radial field is found by solving Laplace's equation above the photosphere, with $\overline{B}_z$ as a boundary condition, and evaluating the result at $z = 0$. This calculation (see Appendix B.) yields

$$\overline{B}_r(x, y, 0) = \overline{B}_r(r) = \sqrt{\frac{\pi^3}{2}} \frac{q_0 N r}{\delta} e^{\frac{-r^2}{4\delta^2}} \left[I_0(\frac{r^2}{4\delta^2}) - I_1(\frac{r^2}{4\delta^2}) \right] \quad , \tag{39}$$

where $q_0 N$ is the total charge in the background field distribution. The $\hat{\mathbf{x}}$ and $\hat{\mathbf{y}}$

components of the total radial field are then

$$B_x(x,y) = \left(\frac{x}{\sqrt{x^2+y^2}}\right)\overline{B}_r(r) + \frac{(x-x_0)}{|(x-x_0)^2+y^2|^{\frac{3}{2}}} \quad (40)$$

$$B_y(x,y) = \left(\frac{y}{\sqrt{x^2+y^2}}\right)\overline{B}_r(r) + \frac{(y)}{|(x-x_0)^2+y^2|^{\frac{3}{2}}} \ , \quad (41)$$

Substituting into the field line equation, $dx/B_x = dy/B_y$, allows us to integrate field lines in the photosphere starting from any point (x,y), given an initial direction $\mathbf{dx} = dx\hat{\mathbf{x}} + dy\hat{\mathbf{y}}$. (We now assume that the test charge is of unit strength; by varying the parameter N appearing in equation (39), we can change the strength of the test charge relative to the background field.)

From the discussion of the Taylor series expansion of the field near a null, we know that the two field lines we want to integrate are locally parallel to that eigenvector of $\mathbf{M}$ which both lies in the $x-y$ plane, and corresponds to one of $\mathbf{M}$'s two negative eigenvalues. Due to the symmetry in this configuration, this amounts to integrating "backwards" from the null beginning in the $\pm\hat{\mathbf{y}}$ directions and ending near the "source" of these two field lines, somewhere near the centroid of the background field, where more vertical "source" flux is found. This is illustrated in Figure 6 for the case of a test charge on the tail of a distribution, at $r_{\text{test}} = 1.5\delta$ from the distribution's centroid, with $N = 100$.

Our next task is to find the normal flux enclosed by these field lines and a circle of radius R. We denote the enclosed flux by $Q_{enc}(R)$, where R is the distance from test charge. In order to capture the dependence of this quantity on R, we integrate $\overline{B}_z$ in annular rings, centered at the test charge, increasing the radius R at each step as shown in Figure 7. In practice, 50 incremental steps in R were taken to ensure smoothness in $Q(R)$.

Probabilistic Arguments

We now possess the machinery to derive a probabilistic measure of the likelihood of the test charge having a separator of length ℓ. For conceptual ease, we now treat the background field as that arising from a collection of N discrete charges. Practically, in a given configuration, we are interested in the length of the separator associated with

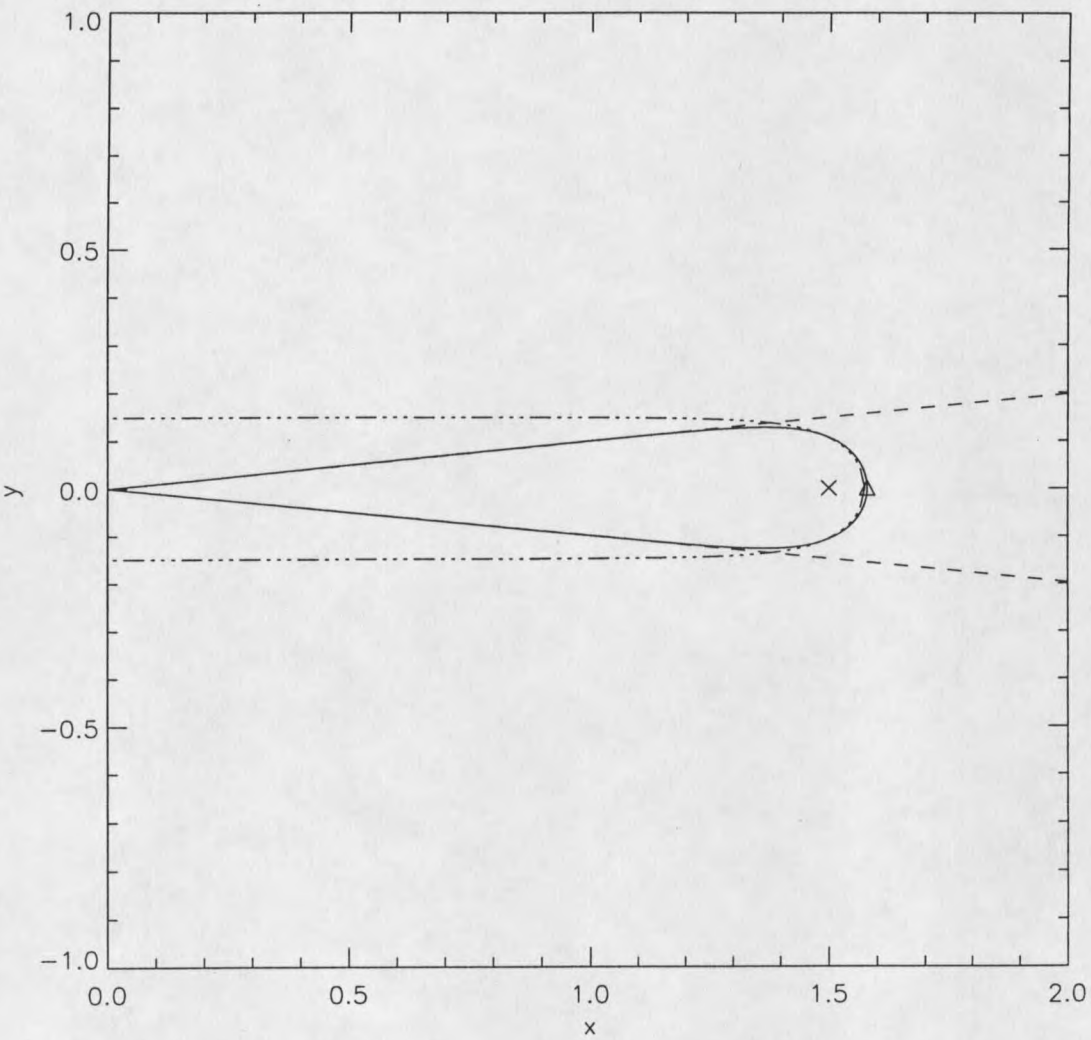


Figure 6: The intersection of the test charge's separatrix with the photosphere $\mathcal{C}_\Sigma$, is plotted (solid) for a background field strength 100 times that of the test charge. The test charge is located at a distance $r_{\text{test}} = 1.5$ from the centroid of the background field, in units of δ, the width of the Gaussian background field. Also plotted are the the radial asymptotes of the field lines as they near the origin (dashed), and the separatrix of a test charge in a uniform background field (dash - dot) of strength $B_0 = \overline{B}_z(1.5\delta)$. The test charge's location is marked with an (x), and the test charge's null is marked with a ($\triangle$). The null would be at nearly the same place if the background field were uniform. Both axes are in units of δ.

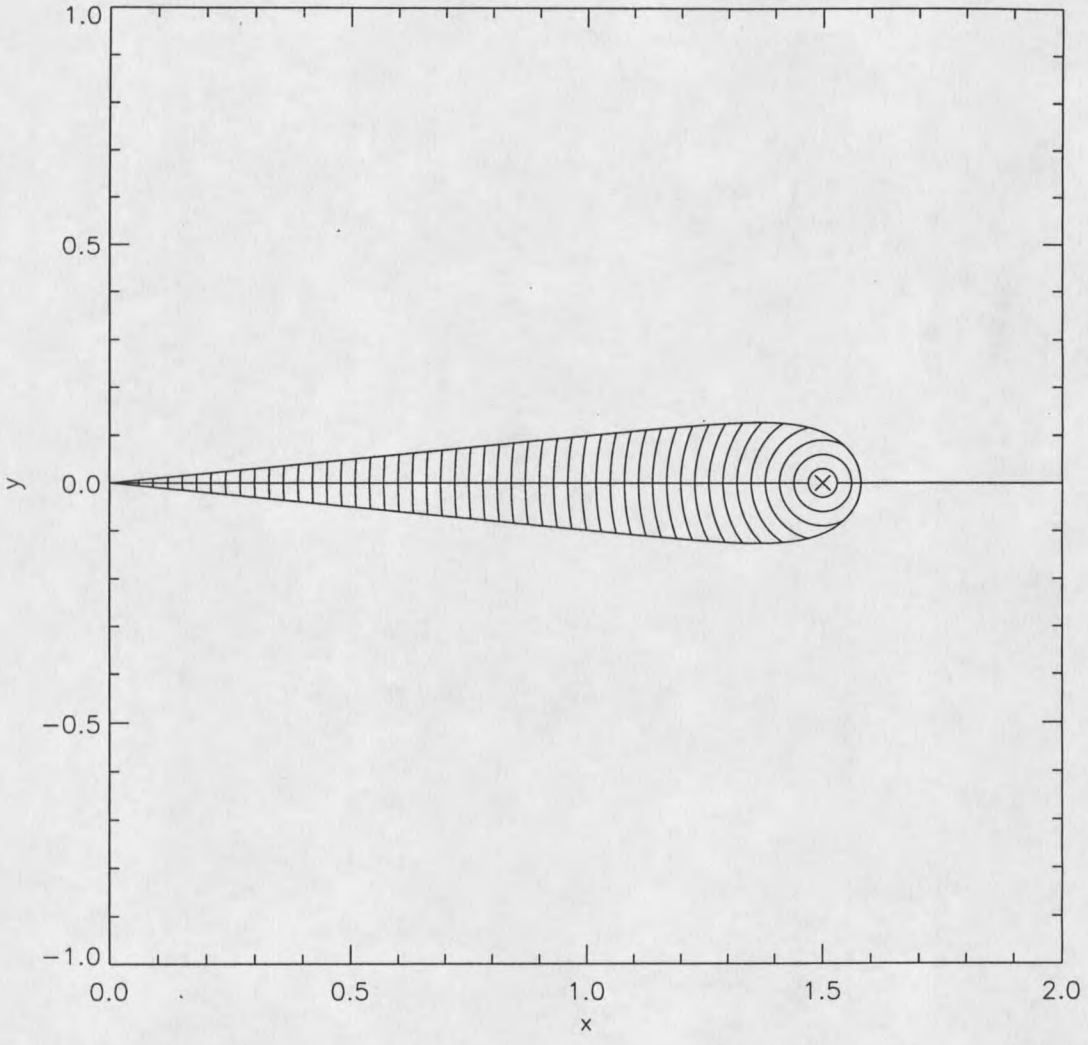


Figure 7: The normal flux, $\overline{B}_z$, enclosed by $\mathcal{C}_\Sigma$, the intersection of the test charge's separatrix with the photosphere, is integrated in annular rings, centered on the test charge, for the case shown in the previous figure. Both axes are in units of δ.

the test charge and the closest field charge. This is because the self-inductance of the shortest separator in the configuration will be the least, meaning currents are most easily induced along it. (Recall that, for fixed flux, current is inversely proportional to self-inductance.) Hence, while photospheric motions alter the flux through all of the configuration's separators, the shortest is the most likely site of transient brightenings.

Accordingly, we focus the following development on finding the field charge closest to the test charge, which, in turn, can be used to determine the length of the shortest separator. As discussed above, the probability of the test charge sharing a separator with a field charge must be directly related to the probability of its sharing flux with that charge.

We begin by considering the probability of $\mathcal{C}_\Sigma$ *not* enclosing a field charge within a distance R of the test charge. Since the location of every charge obeys the same probability distribution, i.e., the Gaussian distribution assumed above, this is simply

$$P_0(R) = \left[1 - \frac{Q_{enc}(R)}{Q_{tot}}\right]^N , \tag{42}$$

where $Q_{tot} = q_0 N$ is the total magnetic charge in the distribution of N background charges. Since the event of *having* "hit" a charge and not having hit one are mutually exclusive, the probability of the former must be unity minus that of the latter,

$$P(R) = 1 - P_0(R) = 1 - \left[1 - \frac{Q_{enc}(R)}{Q_{tot}}\right]^N . \tag{43}$$

Next, to account for the possibility that another charge might not be encountered at all, we employ Bayes' theorem (Press et al. 1988), and define

$$\begin{aligned} \tilde{P}(R) &\equiv P(R|R_{\max}) = \frac{P(R_{\max}|R)P(R)}{P(R_{\max})} \\ &= \frac{1 - \left[1 - \frac{Q_{enc}(R)}{Q_{tot}}\right]^N}{1 - \left[1 - \frac{Q_{enc}(R_{\max})}{Q_{tot}}\right]^N} , \end{aligned} \tag{44}$$

which is the probability that there is at least one field charge within a distance R of the test charge, given that there is at least one field charge within the separatrix. Here, $R_{\max}$ is the point on $\mathcal{C}_\Sigma$ furthest from the test charge. In Figures 8 and 9, we

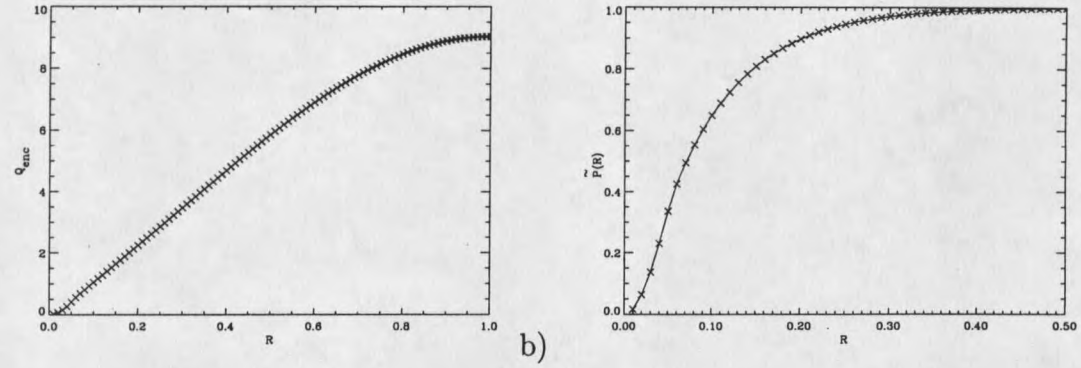


Figure 8: a) $Q_{\rm enc}(R)$, the vertical flux $\overline{B}_z$ enclosed by $\mathcal{C}_\Sigma$ within a distance R of the test charge, plotted as a function of R. b) $\tilde{P}(R)$, the probability that a field charge has been encountered within R of the test charge, given that $\mathcal{C}_\Sigma$ encloses a field charge, as a function of R. The abscissae are in units of δ, the Gaussian's width. Here, $N = 100$, and $r_{\rm test} = 1.0$.

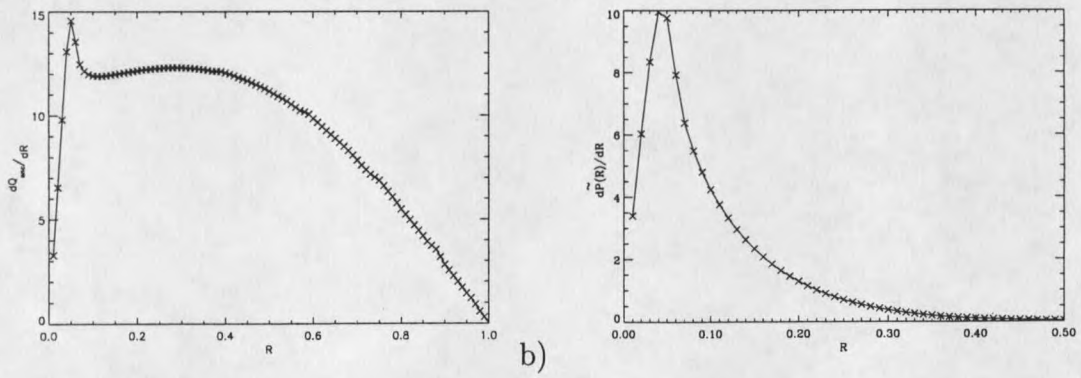


Figure 9: a) $dQ_{\rm enc}(R)/dR$, computed using a first-order, three-point, centered difference approximation, plotted here against R, for the same case as in the previous figure. b) $d\tilde{P}(R)/dR$, computed with the same method, versus R.

plot several of the quantities appearing in these calculations, for a particular choice of N and r_{test}. For these plots, 100 steps were taken in R to ensure smoothness in the plotted curves (nominally, 50 steps in R were taken).

The normed expectation value of a quantity F(R) can be determined from the differential probability distribution,

$$\langle F \rangle = \frac{\int_0^{R_{\max}} dR \frac{d\tilde{P}(R)}{dR} F(R)}{\int_0^{R_{\max}} dR \frac{d\tilde{P}(R)}{dR}} = \int_0^{R_{\max}} dR \frac{d\tilde{P}(R)}{dR} F(R) \quad . \tag{45}$$

Similarly, the standard deviation can be defined

$$\Delta F = \sqrt{\langle F^2 \rangle - \langle F \rangle^2} \quad . \tag{46}$$

Thus, we have a prescription for calculating the expected distance from the test

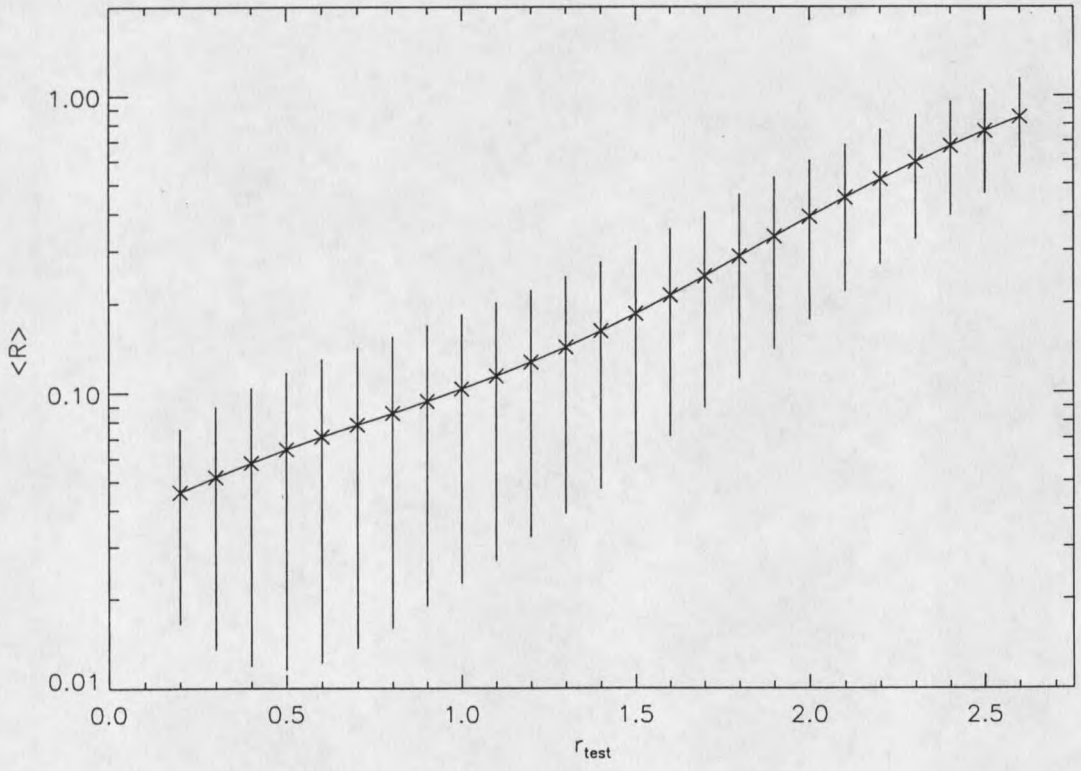


Figure 10: A plot of $\langle R \rangle$ and its standard deviation ΔR, as the distance r_{test} from the test charge to the centroid of the Gaussian background field is varied. Both the ordinate and abscissa are in units of δ, the Gaussian's width. The background field is 100 times as strong as the test charge.

charge to the nearest field charge, $\langle R \rangle$, and its standard deviation ΔR. In Figure 10, we have plotted these quantities, as the distance $r_{\rm test}$ from the centroid of the background field to the test charge is varied.

While $\langle R \rangle$ is the distance between the test charge and the closest field charge with which it shares flux, we really want the distance between these charges' nulls. Accordingly, we must modify this result to reflect test null - field null separation, instead of test charge - field charge separation. We account for the difference by adding the expected charge-null separation distances (cf., equation (6))

$$\Delta_{\rm charge-null}(r_{\rm test}) = \sqrt{q_B/\overline{B}_r(r_{\rm test})} \tag{47}$$

$$\Delta_{\rm charge-null}(r_{\rm test} - \langle R \rangle) = \sqrt{q_B/\overline{B}_r(r_{\rm test} - \langle R \rangle)} \tag{48}$$

to $\langle R \rangle$. We denote this new quantity $\langle R_{AB} \rangle$,

$$\langle R_{AB} \rangle = \langle R \rangle + \Delta_{\rm charge-null}(r_{\rm test} - \langle R \rangle) + \Delta_{\rm charge-test}(r_{\rm test}) \tag{49}$$

To determine the standard deviation in the null-null distance from the charge-charge distance, we Taylor expand the expected field null - field charge separation,

$$\Delta_{\rm charge-null}(r_{\rm test} - \langle R \rangle) \ , \tag{50}$$

to determine its dependence upon ΔR, which gives, to first order in ΔR,

$$\sqrt{q_B/\overline{B}_r(r_{\rm test} - (\langle R \rangle \pm \Delta R))} \simeq \sqrt{q_B/\overline{B}_r(r_{\rm test} - \langle R \rangle)}\left(1 \mp \frac{B'(r_{\rm test} - \langle R \rangle)}{2B(r_{\rm test} - \langle R \rangle)}\Delta R\right) \tag{51}$$

Since the background field is well-behaved, we take $(B'/B) \sim 1/\delta = 1$, implying that the variation in the null-charge distance is roughly half the standard deviation of the charge-charge distance. Accordingly, we approximate $\Delta R_{AB} = 1.5\Delta R$. For comparison, we have plotted the two distances in Figure 11, as the distance $r_{\rm test}$ from the centroid of the background field to the test charge is varied. The increase in $\langle R_{AB} \rangle$ for small $r_{\rm test}$ is an artifact of the symmetry in the background field: near the distribution's centroid, the radial field B_r vanishes, which increases the field charge-field null distance $\sqrt{q_B/\overline{B}_r(r_{\rm test} - \langle R \rangle)}$ added to $\langle R \rangle$ to get $\langle R_{AB} \rangle$, as $(r_{\rm test} - \langle R \rangle)$ approaches zero.

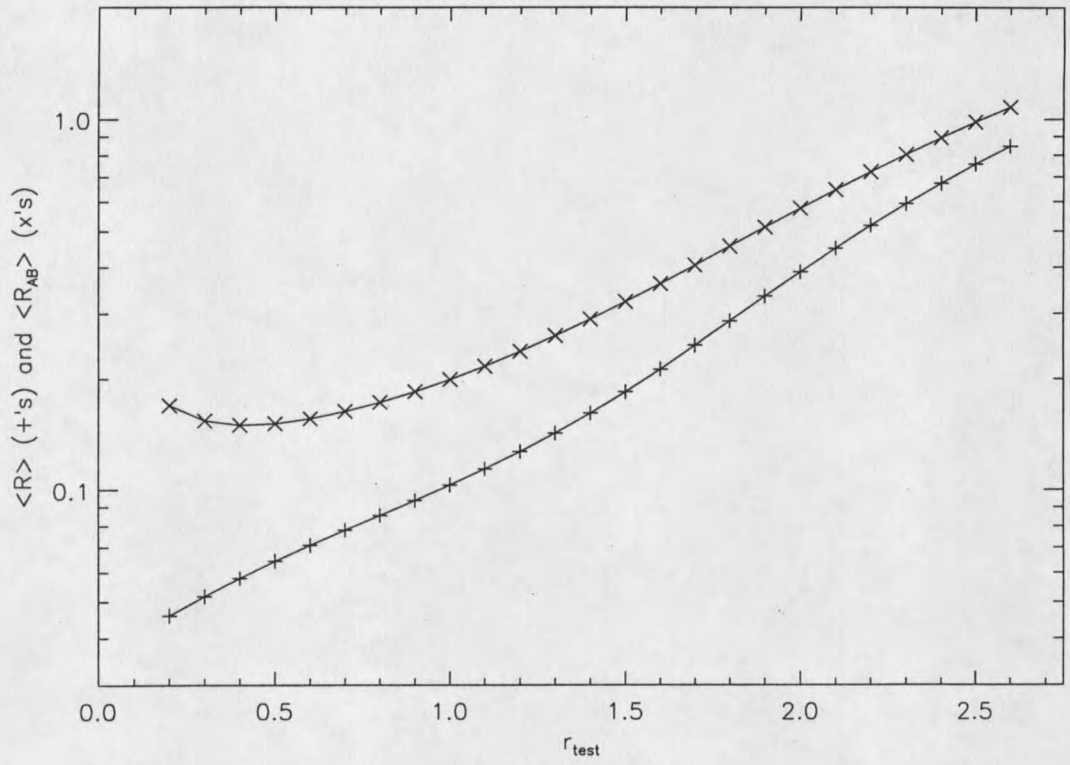


Figure 11: A plot of the null-to-null distance $\langle R_{AB} \rangle$ (x's) and the charge-to-charge distance $\langle R \rangle$ (+'s), as the distance r_{test} from the test charge to the centroid of the Gaussian background field is varied. As in the previous figure, both the ordinate and abscissa are in units of δ, and the background field is 100 times as strong as the test charge. The increase in $\langle R_{AB} \rangle$ for small test charge distances is an artifact of the background field's symmetry.

We make the simplifying assumption that the separator is a semicircular loop running through the corona, in a plane perpendicular to the photosphere, from the field charge's null to the test charge's null. Hence, we can find the expected separator length $\langle \ell \rangle$ by multiplying the distance between the nulls, $\langle R_{AB} \rangle$, by $(\pi/2)$.

Results

The most useful results of this work will be statistical predictions of the lengths of coronal X-ray loops, as determined by a few simple parameters that can be used to characterize an active region — size, net flux, and the number of its constituent photospheric flux elements. It is also reasonable to expect that the length of such loops should depend upon their connectivity within the active region: loops with a footpoint at a flux element nearer the center of the active region, where the magnetic field geometry is more complex and field strengths are stronger, are presumably shorter, on average, than loops on the fringes of the active region, where the magnetic features that share flux are further apart. Simply put, since our hypothesis is that nulls form the footpoints of loops, and the density of nulls is less where the density of charges is less, loops should be longer when their footpoints are further away from the distribution's centroid.

To illuminate the dependence of loop lengths upon these parameters, we used the procedures outlined above to calculate $\langle \ell \rangle$ and $\Delta \ell$, as a function of the location of the test charge relative to the background field's centroid, and, separately, as a function of the strength of the test charge relative to the total flux in the background field. It should be emphasized that, since this entire development follows from finding the shortest distance to a field charge with which the test charge shares flux, $\langle \ell \rangle$ is the expected length of the *shortest* separator. In Figure 12, we show $\langle \ell \rangle$ and $\Delta \ell$ as r_{test} is varied on a linear-log plot. The background field is kept at a constant value, with 100 times the flux of the test charge. This plot strongly suggests that $\langle \ell \rangle$ has an exponential dependence on r_{test}. We expect that the true exponential dependence on r_{test} is in $\langle R \rangle$, since $\langle \ell \rangle$ has a complicated dependence on r_{test} due to the charge-charge to null-null distance conversion. Accordingly, a χ^2-minimization using a nonlinear,

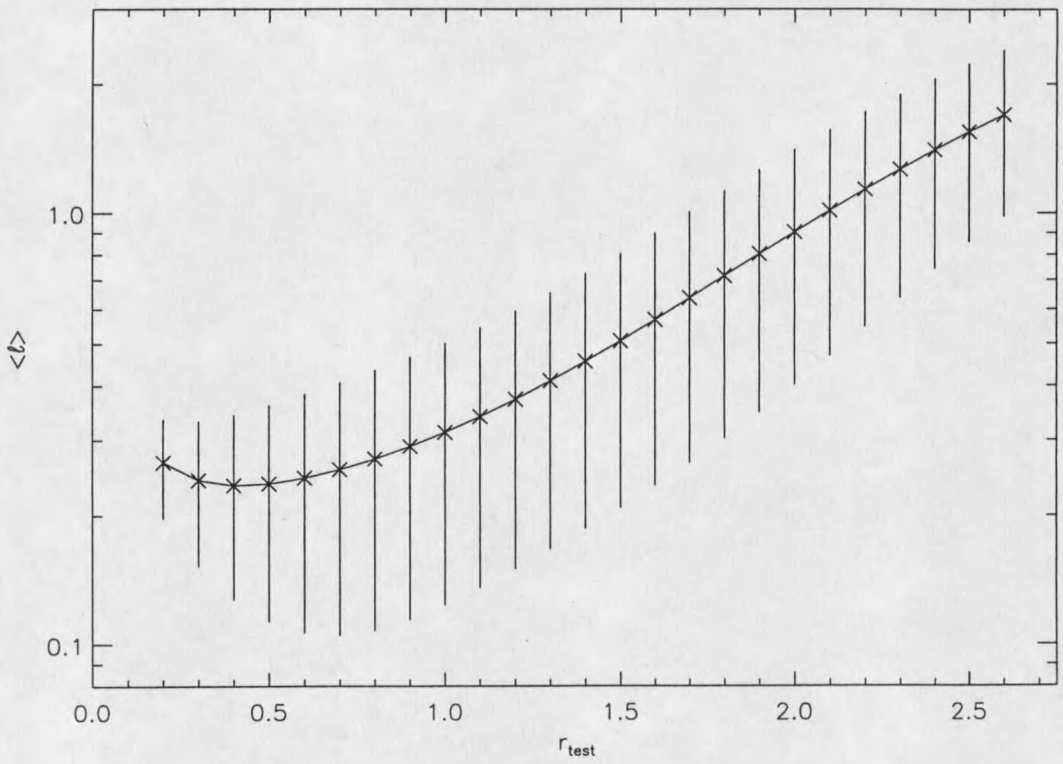


Figure 12: A plot of $\langle \ell \rangle$ and $\Delta \ell$ as the distance between the test charge and background field's centroid, r_{test}, is varied. The background field is fixed at 100 times the strength of the test charge. Both abscissa and ordinate are in units of δ, though the latter is on a logarithmic scale.

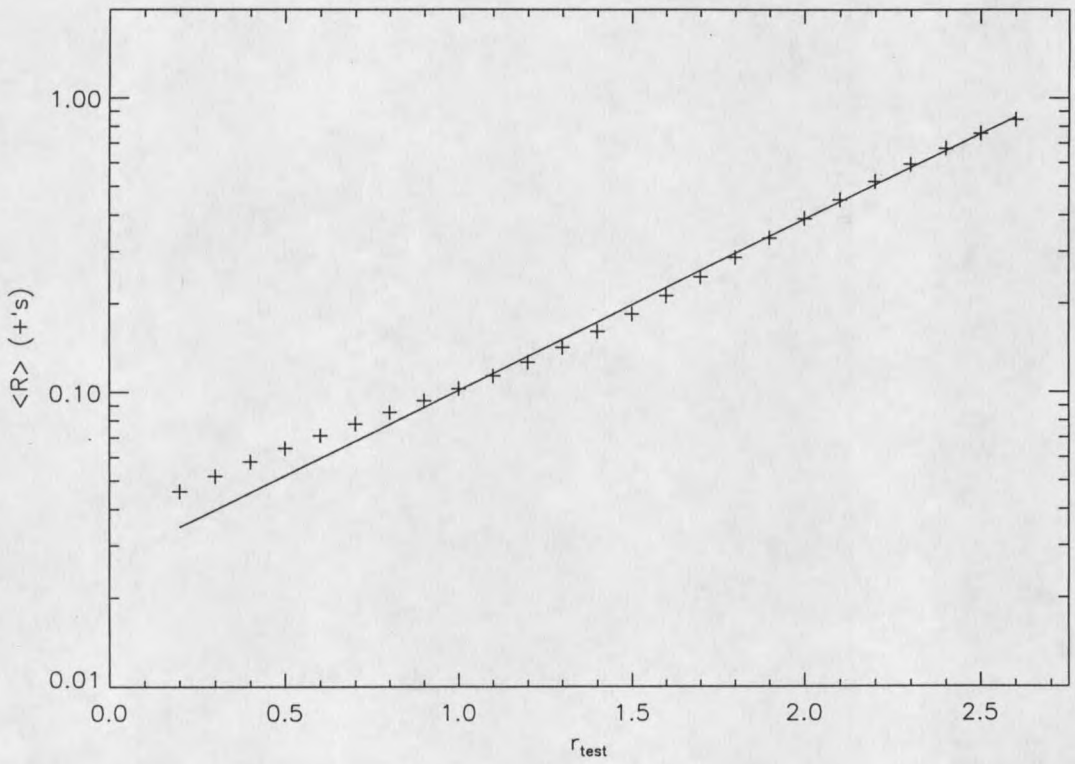


Figure 13: A plot of $\langle R \rangle$ (x's) and a χ^2-minimization of a exponential fit to $\langle R \rangle$ (solid) as r_{test} is varied, with the same background field strength as in the previous figure. Again, both abscissa and ordinate are in units of δ, with the latter on a logarithmic scale.

least-squares routine yields $\langle R \rangle = .027 \exp(1.34 r_{\text{test}})$. This fit to $\langle R \rangle$ is shown in Figure 13. Evidently, $\langle R \rangle$, and hence $\langle \ell \rangle$, scale, roughly, as $\exp(4 r_{\text{test}}/3)$.

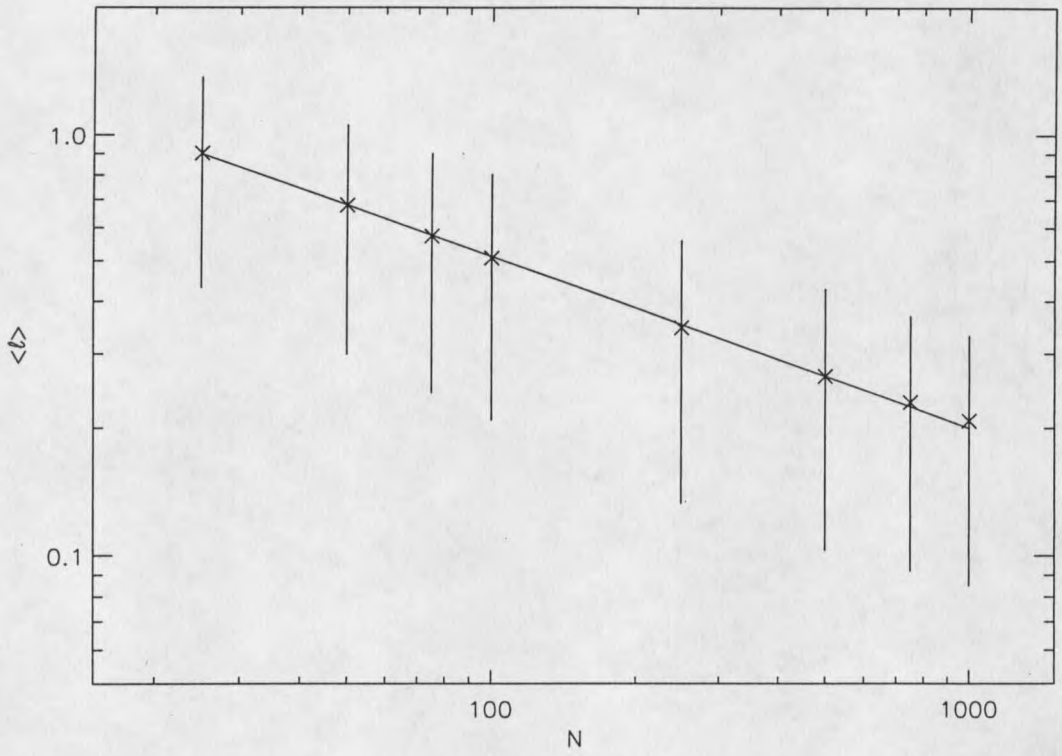


Figure 14: A plot of $\langle \ell \rangle$ (x's) and $\Delta \ell$ as N is varied, with r_{test} held fixed at 1.5δ. A power-law fit is also plotted (solid). The abscissa is in units of the test charge's flux, while the ordinate is in units of δ; both scales are logarithmic.

In Figure 14, we show, on a log-log plot, $\langle \ell \rangle$ and $\Delta \ell$ as the strength N of the background field, relative to that of the test charge, is varied, while r_{test} is held fixed at 1.5δ. A power-law fit of $\langle \ell \rangle$ as a function of N is also plotted. (In contrast to the previous case, we expect $\langle \ell \rangle$ itself to exhibit the power-law dependence, as the variation in background field strength affects the charge-charge to null-null distance conversion linearly.) The χ^2-minimization gives $\langle \ell \rangle = 3.3(N^{-.47})$. As another rough approximation, then, $\langle \ell \rangle$ scales as $\sim 1/\sqrt{N}$.

It is worth remarking that the "opening angle" of $\mathcal{C}_\Sigma$, defined as twice the inverse tangent of the slope of one of its "asymptotic" field lines (see Figure 6), exhibits a similar dependence: a fit of the half the opening angle, assuming a power law, gives

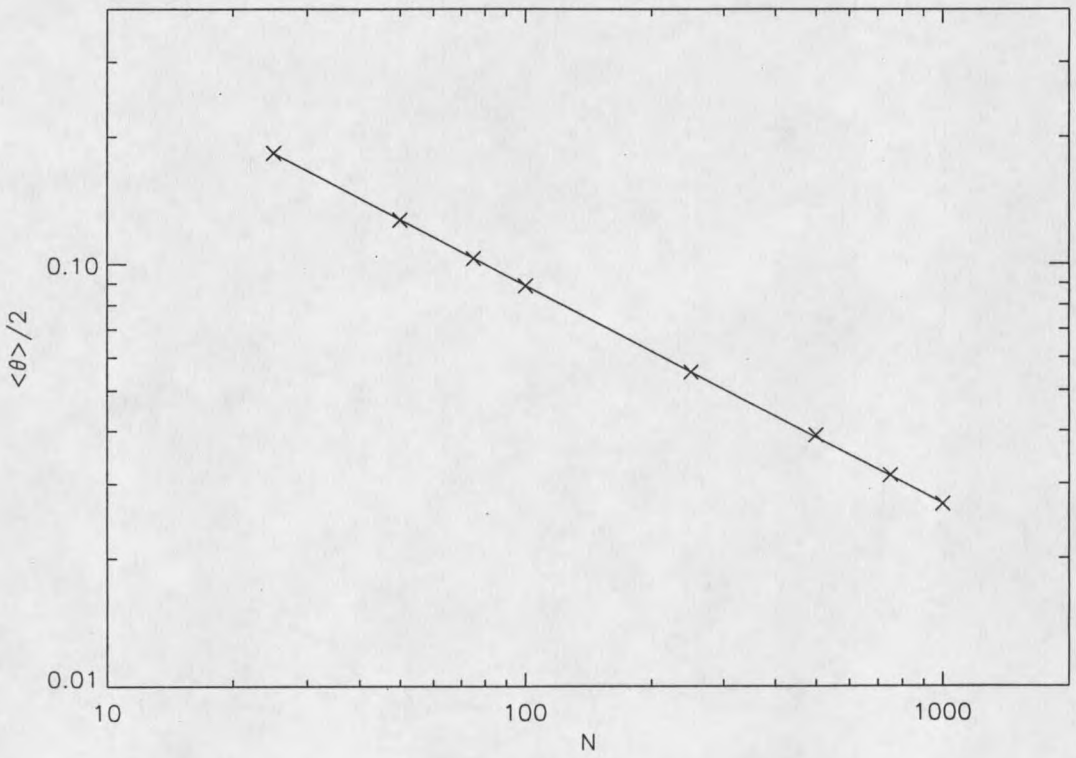


Figure 15: A plot of the half of $\mathcal{C}_\Sigma$'s "opening angle" (see Figure 6), $\langle\theta\rangle/2$ (x's), and the χ^2-minimization of a power-law fit (solid), as background field strength N is varied. As before, r_{test} is held fixed at 1.5δ. The abscissa is, as above, in units of the test charge's flux, while the ordinate is in radians; both scales are logarithmic.

$\langle\theta\rangle/2 = .97(N^{-.52})$, as shown in Figure 15. No simple relation is apparent between the opening angle and r_{test}.

CHAPTER 4

Active Regions Composed of Discrete Flux Elements

To test the results of the analytic scheme of the previous chapter, we now ignore the ensemble averaging employed there, and work directly with fields that arise from a distribution of discrete flux elements. Finding separator lengths in this case involves a fundamentally different approach. We confine our discussion to configurations with N magnetic "field" charges, all of like sign, and one "test" charge of opposite sign. For concreteness, we take the field charges to be positive.

Methods

As a starting point, we consider the topological properties of such configurations. Given $(N+1)$ charges, there are N generic nulls, of which $(N-1)$ are B-type and one is A-type. Since a separator must run from a B-type null to an A-type null, $N \geq 2$ is a necessary condition for a separator to exist. Since the existence of a separator further requires that a field charge's separatrix intersect the test charge's separatrix, a sufficient condition for the existence of a separator is that the test charge share flux with more than one field charge, which depends upon the details of a given configuration. (For a localized charge distribution, the only circumstance in which this cannot happen is that in which the sole field charge that shares flux with the test charge is stronger than the test charge, such that latter's separatrix would be contained entirely within the separatrix of the former.) To generalize, if the test charge shares flux with n field charges, there are only $(n-1)$ separators; in every case, the flux shared between the test charge and exactly one of the field charges is not encircled by a separator.

If the test charge shares flux with n of the configuration's N field charges, we must find the lengths of $(n-1)$ separators. From the definition of a separatrix, we know

that all of the test charge's field lines must begin along or within $\mathcal{C}_\Sigma$, the intersection of the test charge's separatrix and the photosphere. Hence, the n field charges and $(n-1)$ nulls must lie on the boundary of, or within, the area eclosed by $\mathcal{C}_\Sigma$. This irregularly-shaped area has been termed the test charge's "footprint." In Figure 16,

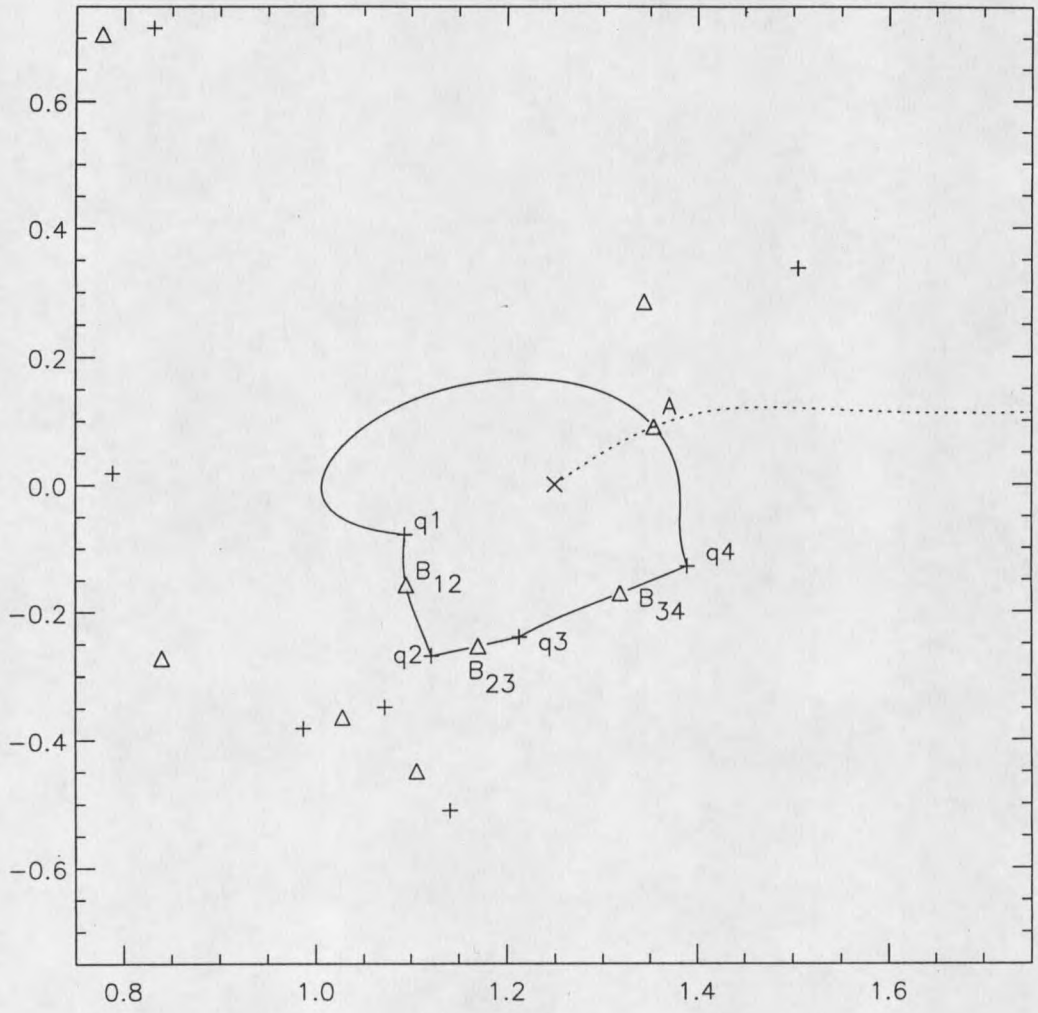


Figure 16: A test charge's "footprint," the area bounded by $\mathcal{C}_\Sigma$, the intersection of the test charge's separatrix and the photosphere (solid). Also shown are the A-type null's two γ-lines (dotted): one runs from A to the test charge at x, while the other runs to $+\infty$. Here, $r_{\text{test}} = 1.25\delta$ and $N = 100$.

we show an example of a footprint. Notice the topological structure of $\mathcal{C}_\Sigma$: from the test charge's A-type null, labeled A, two separatrix field lines run to field charges $q1$

and $q4$; from these charges, γ-lines run to the field nulls B_{12} and B_{34}; other γ-lines run to these nulls from the field charges $q2$ and $q3$; finally, γ-lines from these last two charges converge on the field null B_{23}.

As in the previous chapter, we assume that the separators are semicircular loops running through the corona from field null to test null. Since all nulls are assumed generic, the null associated with the test charge is the only A-type null in the configuration, which means all the separators have one end at this null. All of the B-type nulls at these separators' opposite ends lie along or within $\mathcal{C}_\Sigma$. This means we can find the separators' lengths by finding the distance between the two nulls at each separator's endpoints, and multiplying the result by $\pi/2$.

Accordingly, we must determine the locations of the $(n-1)$ B-type nulls associated with the n field charges that share flux with the test charge, as well as the location of the A-type null. Hence, we seek the locations of exactly n nulls. Finding the test charge's null is straightforward, as its approximate location is known and its type is certain: Newton's method in two-dimensions suffices.

Finding the separators' other nulls, in contrast, is difficult. One approach is to try to find all of the N nulls in the configuration of $(N+1)$ charges, and then to integrate γ-lines from the test charge's null to two field charges. From there, γ-lines from nearby nulls could be integrated to find the null associated with the appropriate field charge; then *that* null's other γ-line can be integrated to the next charge along $\mathcal{C}_\Sigma$. In this way, one could then integrate all the way around $\mathcal{C}_\Sigma$, from null, to charge, to null, etc. In practice, with $N = 100$, only $\approx 70\%$ of the nulls could be found outright using a two-dimensional Newton-Raphson method, and writing a "fire and forget" routine that integrated around $\mathcal{C}_\Sigma$ in such a way would have been a formidable task.

Instead of attempting to find all of the configuration's nulls, the approach adopted here is to try to find only the $(n-1)$ field nulls associated with the n field charges that share flux with the test charge. A first step toward finding the relevant nulls is to find these relevant charges. To this end, an automated routine that integrates field lines from the test charge in the photosphere was written. The integrations start in different directions from the test charge, in angular steps, proceeding counter-

clockwise. When the integrator finds field lines with endpoints at different charges on either side of an angular interval, the interval is subdivided, and a field line is integrated in the intermediate direction. Whichever side of this "fork" contains field lines from differing field charges is subdivided again, until the angular width of the subdivided interval is $(\frac{1}{2})^{20}$ of the initial angular step, $\frac{2\pi}{10}$. A full 2π radians are integrated around the test charge, in this way finding, it is assumed, all the field charges on or within $\mathcal{C}_\Sigma$. The resulting plot of photospheric field lines integrated

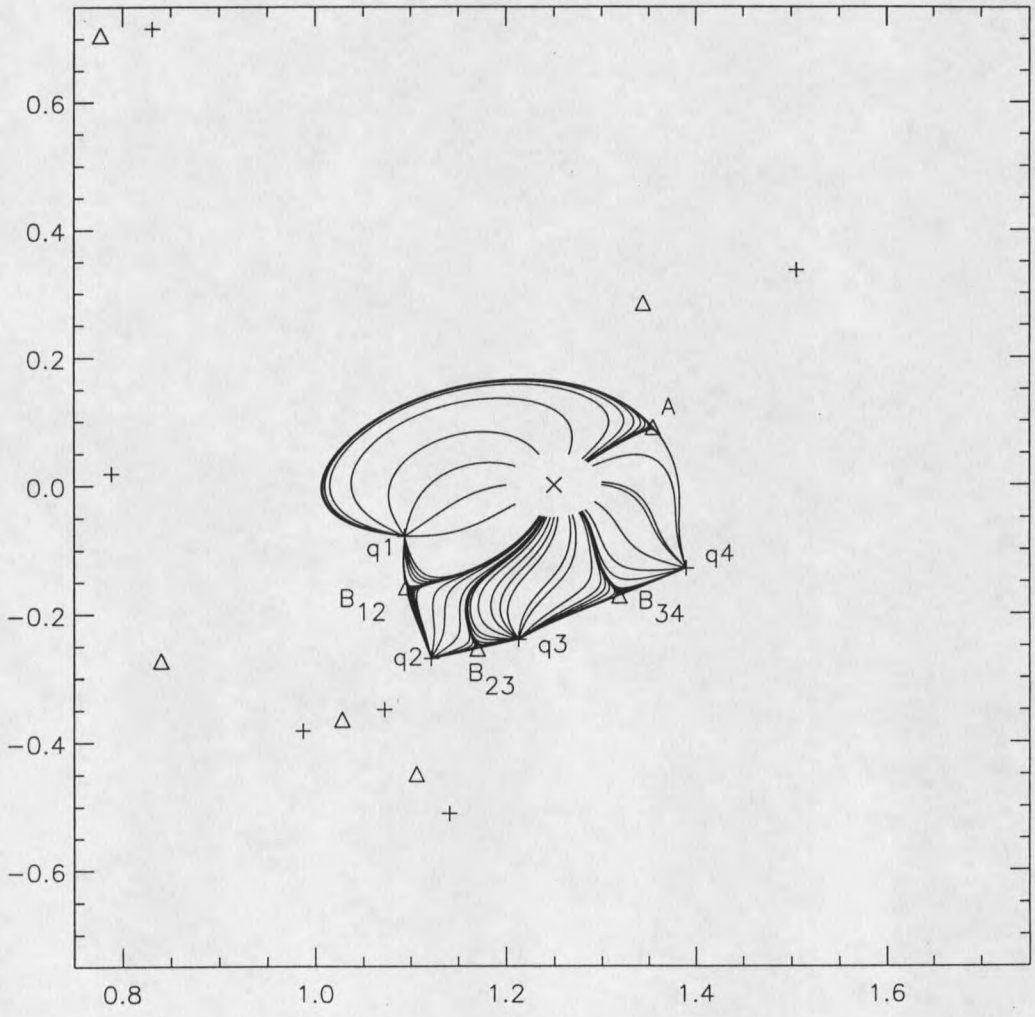


Figure 17: A plot of photospheric field lines (those at $z = 0$) that join the test charge to the field charges with which it shares flux. This footprint is the same as that in the previous figure.

from a test charge to the field charges with which it shares flux clearly displays the structure of that test charge's footprint, as seen in Figure 17. Note the high density of integrated field lines along boundaries between regions of differing connectivity. We call the two integrated field lines that run to distinct field charges and leave the test charge with the smallest angular separation "bisector" field lines.

With the locations of those charges with which the test charge shares flux in hand, it remains to find the B-type nulls whose γ-lines connect to these charges. Information gleaned from the field line integrator as it traces out the footprint can be used to make initial guesses about the nulls' locations, for input to a Newton-Raphson null finder. Specifically, five points recorded by the integrator as guesses for each null's location are useful:

1. The point midway between the pair of charges whose γ-lines run into the null. In the absence of other charges, this would be the exact location of the null.

2. The point at which the rate of growth in separation between the two bisector field lines is greatest. This captures the expected behavior of the field lines near the null: they approach the null in the same direction, but leave in opposite directions along (parallel or antiparallel) to the same eigenvector.

3. The point at which, along the last integrated bisector, the curvature was greatest. This takes advantage of the fact that, at a generic null, the incoming eigenvectors are perpendicular to the outgoing ones, meaning field lines passing close to the null have a 90° "kink" in them.

4. The point at which, along the same bisector, the step size is least, since the integrator's step sizes grow smaller in regions of weak field.

5. The point at which, along the same bisector, the field was minimal.

In many cases, the null finder, fed these initial guesses for a null's location, does not converge to the null sought. One reason for this is that the field contains many more nulls than just those on or within $\mathcal{C}_\Sigma$, and the null finder can converge on an "incorrect" null. Also, since the charge distributions are localized, the field is

arbitrarily small far enough from the distribution, which means the null finder can find a field smaller than any threshold by running off to infinity.

To confirm that the null finder has indeed converged to the "correct" null from a given initial guess, one must integrate γ-lines from the null which was found to verify that they run to "correct" pair of charges: those associated with the desired null. If the null found is not associated with these charges, one must feed another guess to the Newton solver and repeat the procedure. (The first two initial guesses above have been found to be, by far, the most likely to converge to the correct null.)

Assuming the locations of all of the nulls in a given footprint are found, the distances between the A-type null and the B-type nulls are easily found, and, as discussed above, the result is multilied by $(\pi/2)$ to yield the separator lengths.

Results

Literally thousands of footprints were studied, using automated procedures to complete the tasks outlined above, as both r_{test} and N were independently varied. For every test charge location and background field strength chosen, at least 50 "good" footprints were analyzed. A "good" footprint is one in which all nulls on or within $\mathcal{C}_\Sigma$ were found, and all of these were of the correct type.

For each good footprint, the locations all the nulls and their corresponding charges were stored, along with the angular interval over which field lines integrated from the test charge reached each field charge. (These quantities will be used in future studies related to heating power.) In addition to recording the total number of good footprints at a particular test charge location and background field strength, the number of cases in which non-generic nulls were found and the number of cases in which not all nulls were found, i.e., failures, were also recorded.

From the nulls' locations that were stored for each footprint, the shortest separator length for each footprint was found by multiplying the shortest field null to test null distance by $\pi/2$ (Figure 18). Using all the footprints studied at each value of r_{test} and N, the average shortest separator length, $\langle \ell \rangle$, and its standard deviation, $\Delta \ell$, were

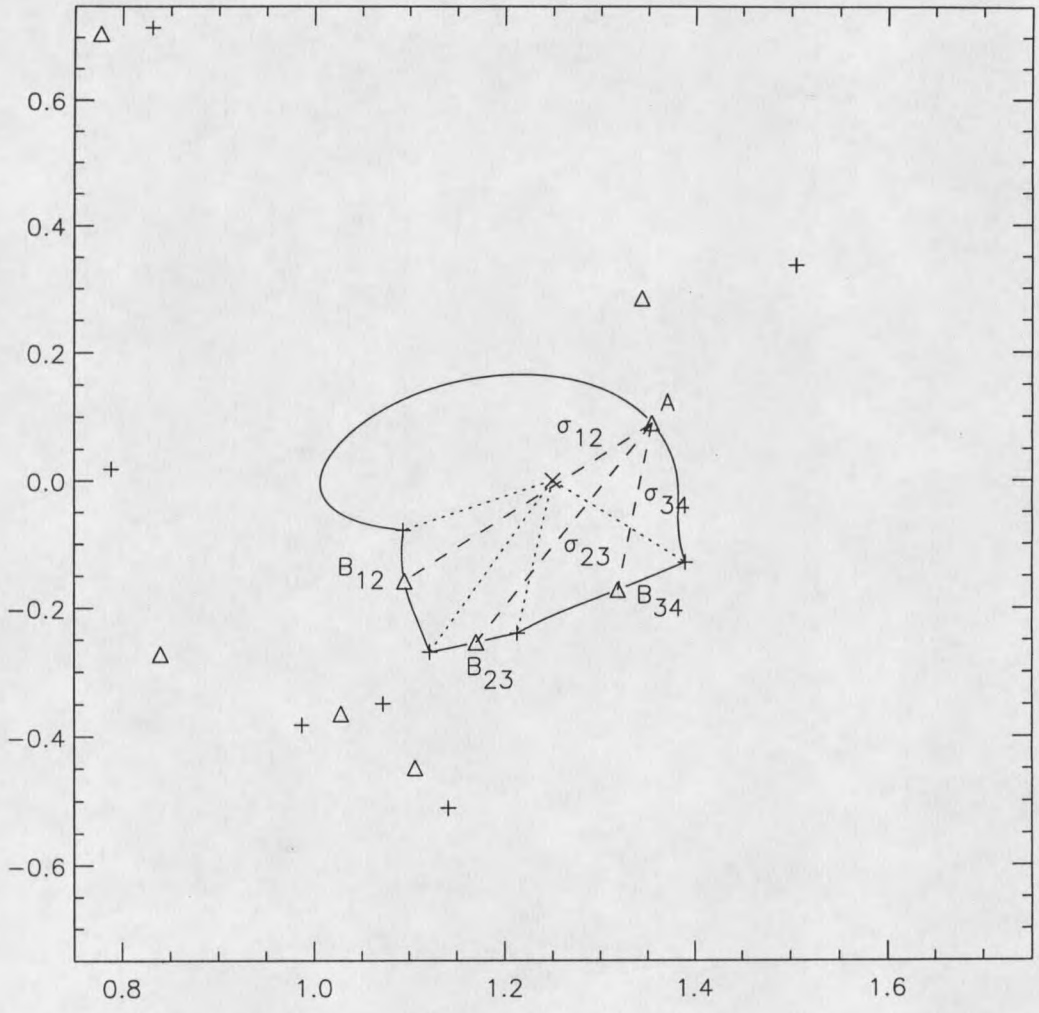


Figure 18: A plot showing the field null - test null distances (dashed) used to find separator lengths. Also shown are field charge - test charge distances (dotted). This is the same footprint appearing in the previous two figures.

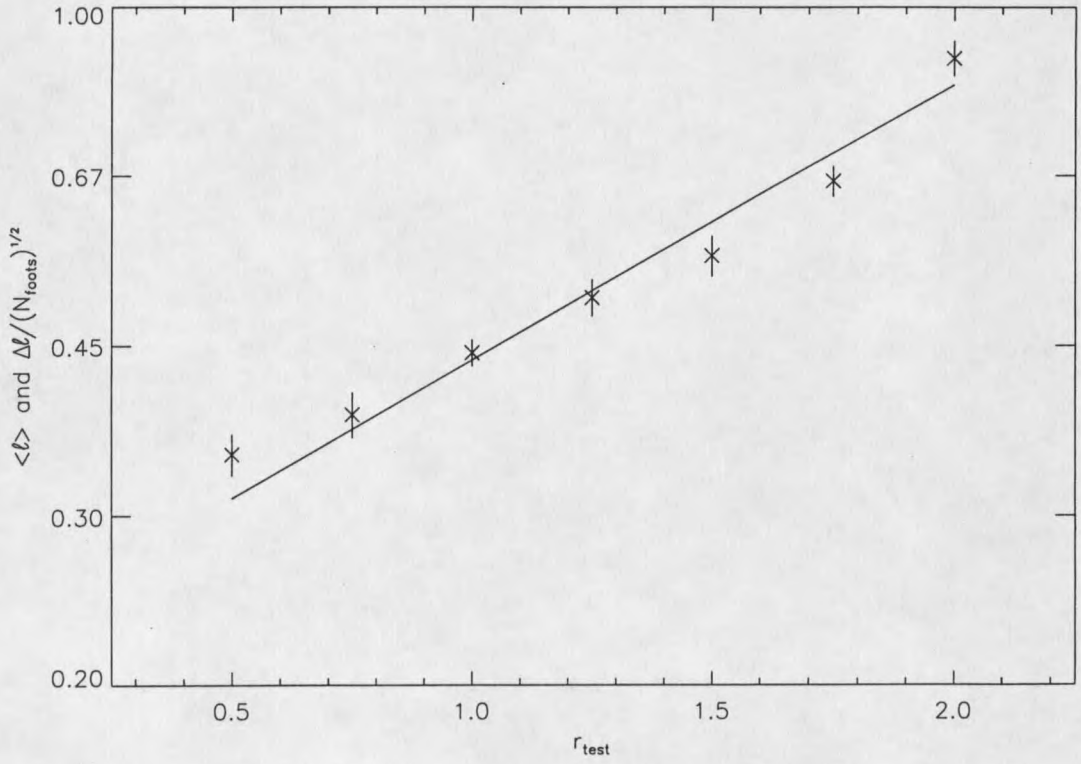


Figure 19: A plot of the shortest separator length in a footprint, $\langle \ell \rangle$, and the standard error in the estimate, $\Delta\ell/\sqrt{N_{\text{footprints}}}$, as r_{test} is varied. An exponential fit is also plotted (solid). N is fixed at 100 flux elements. Both abscissa and ordinate are in units of δ, though the latter is on a logarithmic scale.

then found.

In Figure 19, we show $\langle \ell \rangle$ as r_{test} is varied, as well as the standard error in the estimate, defined to be the standard deviation divided by the square root of the number of trials, i.e., $\Delta\ell/\sqrt{N_{\text{footprints}}}$. The number of background field flux elements, N, is held constant at 100. As in the continuous case, it appears that $\langle \ell \rangle$ depends upon r_{test} exponentially. Another chi-squared minimization yields the result $\langle \ell \rangle = .22 \exp(.65 r_{\text{test}})$. In Figure 20, we show, on a log-log plot, $\langle \ell \rangle$ and $\Delta\ell$ as the number

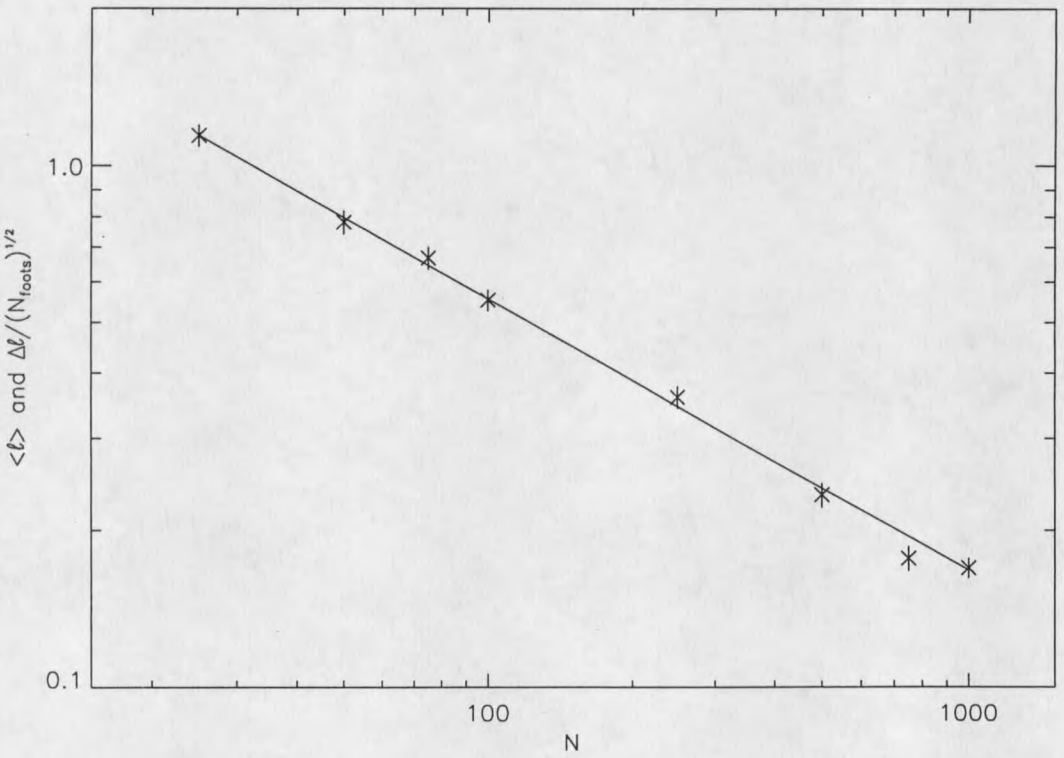


Figure 20: A plot of $\langle \ell \rangle$ and the standard error in the estimate, as the number of charges in the background field, N, is varied, with r_{test} fixed at 1.5δ. A power-law fit to $\langle \ell \rangle$ as a function of N is also plotted (solid). Both ordinate and abscissa are logarithmic.

of charges in the background field, N, is varied, while r_{test} is held fixed at 1.5δ. This plot suggests that, as in the continuous case, $\langle \ell \rangle$ varies as some power of N. A χ^2-minimization gives $\langle \ell \rangle = 6.1(N^{-.52})$. As in the continuous case, then, $\langle \ell \rangle$ scales as $\sim 1/\sqrt{N}$.

For most choices of background field strength and test charge location, the null finder failed to find all the nulls in about 30% of cases. Unfortunately, the likelihood of such failures appears to be correlated with the number of field charges with which the test charge shares flux. Hence, as the density of background charges was increased, the failure rate increased as well. If all the correct nulls were not found, no statistics from that footprint were used in our calculations of separator lengths. This introduces a bias into our results for separator lengths: footprints with more field charges might have longer separators, on average, than those with fewer field charges, and we preferentially compile statistics from the latter.

Practically, however, since we are only interested in the length of the shortest separator, it is believed that the exclusion of footprints in which some of many nulls could not be found should negligibly bias the distribution of the shortest separator lengths.

CHAPTER 5

DISCUSSION

The two approaches outlined in the previous chapters differ greatly in their underlying assumptions. We now compare the results obtained using the two methods. In Figure 21, we plot the expectation values for the length of the shortest separator,

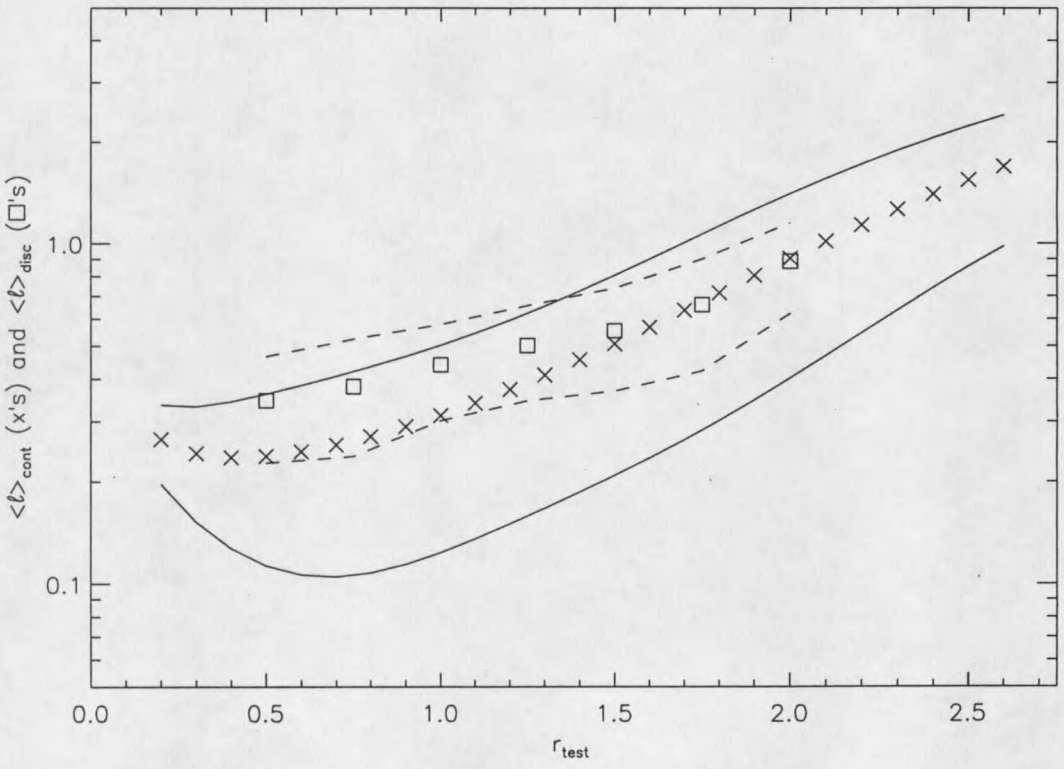


Figure 21: A plot of $\langle \ell \rangle$ found by the continuous field (x's) and discrete (□'s) field approaches, as r_{test} is varied. One σ intervals are also plotted for each case, continuous (solid) and discrete (dashed). Both the ordinate and abscissa are in units of δ, but the latter is logarithmic. The flux in the background field is 100 times the test charge's flux.

$\langle \ell \rangle$, and their standard deviations, obtained by the two methods discussed above, as r_{test} is varied. In Figure 22, we again plot the expectation values for the length of

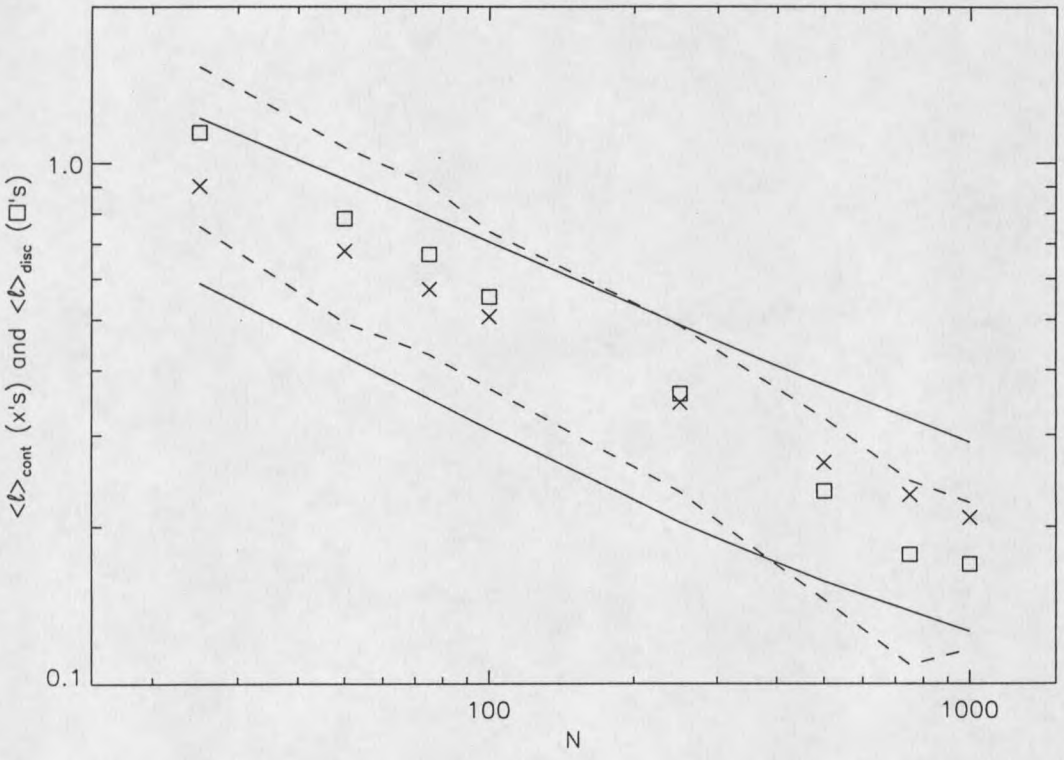


Figure 22: A plot of $\langle \ell \rangle$ as the total flux in the background field is varied, found by the continuous field (x's) and discrete (□'s) field approaches. One σ intervals are also plotted for each case, continuous (solid) and discrete (dashed). The abscissa is in units of the test charge's flux, while the ordinate is in units of δ; both axes are logarithmic. In all cases, $r_{\text{test}} = 1.5$.

the shortest separator, $\langle \ell \rangle$ and the standard deviations obtained using both methods, this time as N is varied.

These results rather unambiguously tell us that separator lengths, as parametrized by N and r_{test}, have a functional dependence of the form

$$\langle \ell \rangle \propto \frac{\exp(\alpha r_{\text{test}})}{\sqrt{N}} \quad , \tag{52}$$

with $\alpha \sim 1$. A comparison with the mean flux element separation λ, where

$$\lambda \equiv \sqrt{\frac{q_0}{\sigma}} = \frac{\exp(\frac{r^2}{4\delta^2})}{\sqrt{N}} \quad , \tag{53}$$

and $\sigma \propto \overline{B}_z$ is the areal "magnetic charge density," shows that intuitive scaling relations are of limited utility in predicting separator lengths.

One thing is clear from these plots: both approaches lead to qualitatively similar results. What is less clear is the degree to which the two methodologies agree quantitatively. One way to investigate the quantitative agreement between the two approaches is to consider the distribution of separator lengths at a particular choice of r_{test} and N. For the continuous case, the only pertinent result available is the differential probability distribution, $d\tilde{P}(R)/dR$ (see Figure 9); we interpret its peak to be the most likely charge separation. Thus, we cannot actually compare two distributions of test null - field null separations. (To "convert" $d\tilde{P}(R)/dR$ into a distribution of null separations, while possible in principle, would introduce the nonlinearities seen in Figure 11.) Instead, we content ourselves with comparing $d\tilde{P}(R)/dR$ with the distribution of charge separations obtained with the discrete-field approach. To the extent that charge separations and null separations are well-correlated (see Figure 23), this is a valid approach.

In Figure 24, we plot both a histogram of charge separations, obtained with the discrete field approach, and the differential probability distribution for test charge - field charge separation, obtained with the continuous field approach. For the case shown, $r_{\text{test}} = 1$, and $N = 100$. Evidently, while average quantities derived with these methods agree reasonably well, differential quantities do not.

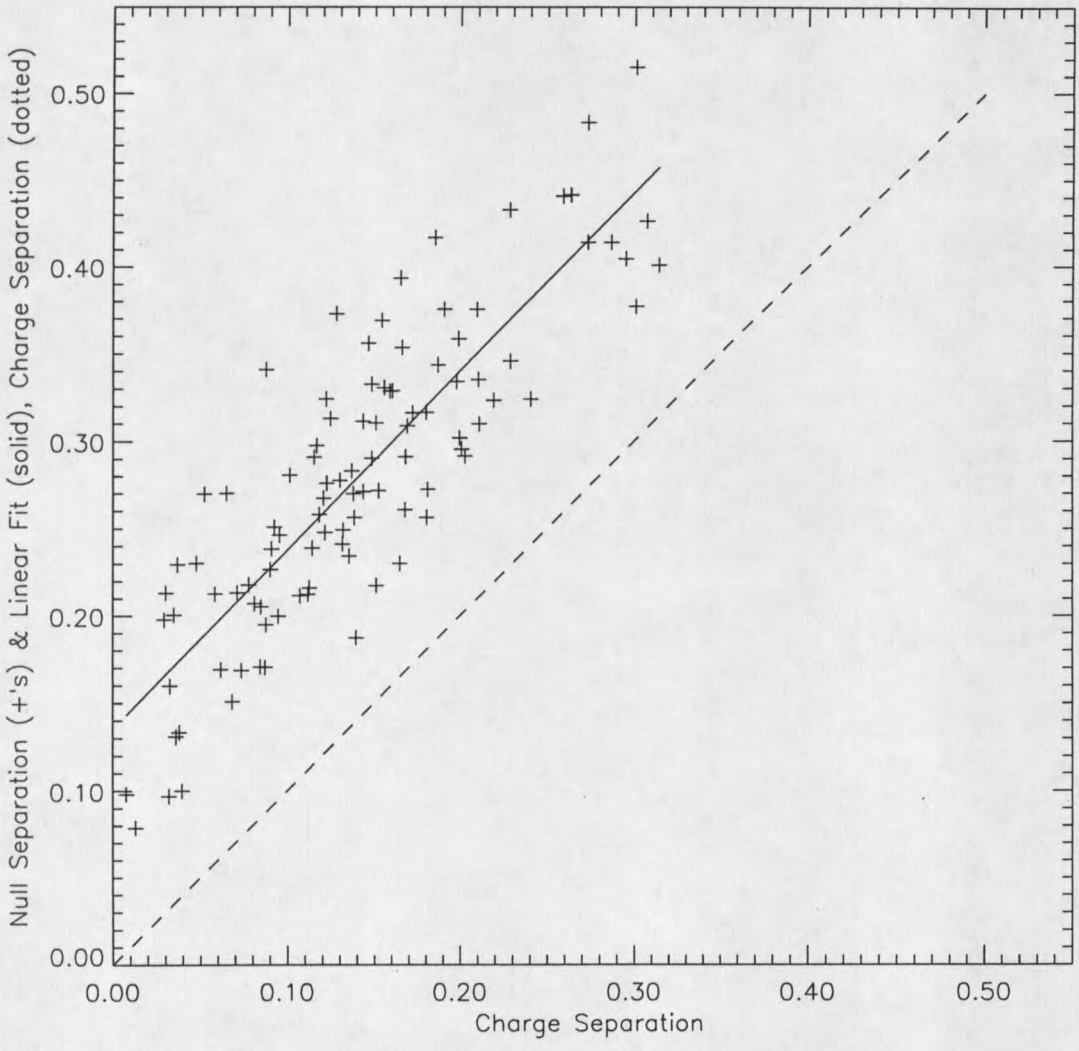


Figure 23: A scatter plot of charge and null separations, obtained with the discrete-field approach. A linear fit is plotted (solid). Note that all null separations are longer than the charge separations, shown with a 45 deg line (dashed). The abscissa and ordinate are in units of δ; $r_{\text{test}} = 1$, and $N = 100$.

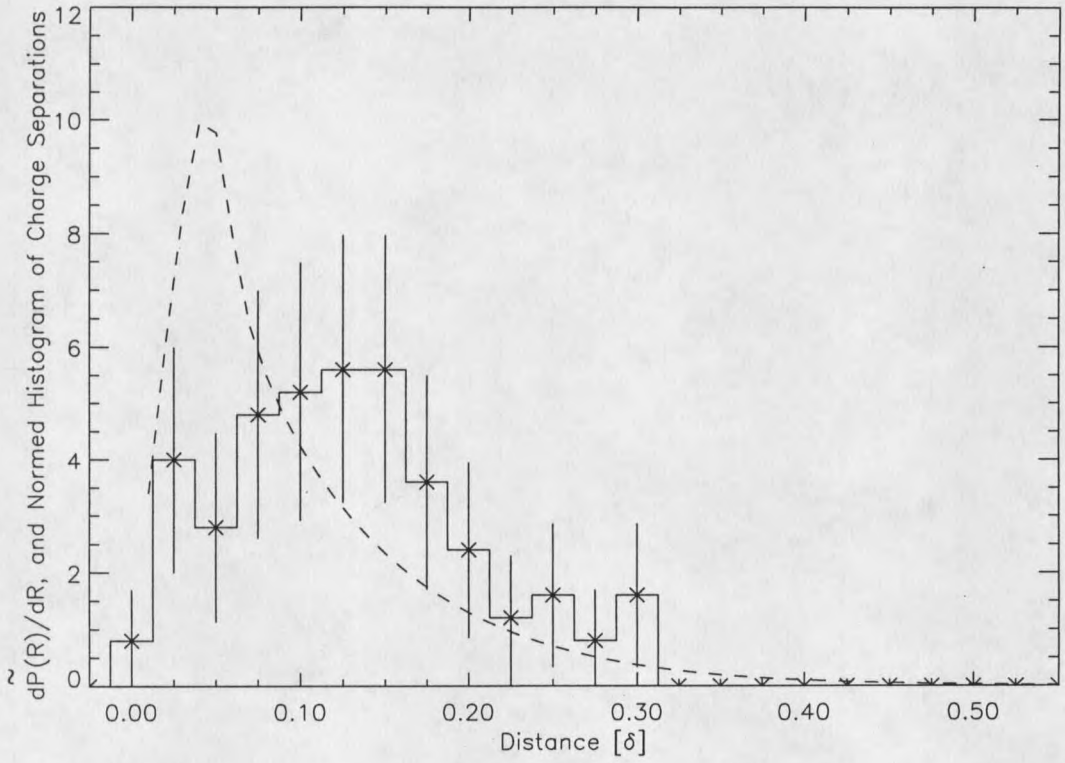


Figure 24: A plot of $d\tilde{P}(R)/dR$ (dashed), obtained with the continuous field approach, and a normalized histogram of charge separations, obtained with the discrete field approach. The abscissa is in units of δ; $r_{\text{test}} = 1$, and $N = 100$.

Appendices

A. A One-Sided Delta Function

Let us consider the properties of the quantity in curly braces in equation (32), which we label $D(r_i, z)$:

$$D(r_i, z) \equiv \frac{z\, r_i}{[r_i^2 + z^2]^{3/2}} \quad . \tag{54}$$

Integrating $D(r_i, z)$ over r_i on the interval $[0, \infty)$ gives unity,

$$\int_0^\infty \frac{z\, r_i\, dr_i}{[r_i^2 + z^2]^{3/2}} = \frac{-z}{[r_i^2 + z^2]^{1/2}}\bigg|_0^\infty = 0 - \left(\frac{-z}{z}\right) = 1 \quad , \tag{55}$$

independent of z.

Observing that $D(0, z) = D(\infty, z) = 0$ we see that, as a function of r_i, $D(r_i, z)$ has a single maximum. Locating it by differentiating,

$$\left.\frac{\partial D(r_i, z)}{\partial r_i}\right|_{r_{\max}} = 0 = \frac{z}{[(r_{\max})^2 + z^2]^{3/2}} + \frac{3\, z\, r_{\max}^2}{[(r_{\max})^2 + z^2]^{5/2}} \tag{56}$$

$$0 = z^2 + r_{\max}^2 - 3r_{\max}^2 \tag{57}$$

$$r_{\max} = \frac{z}{\sqrt{2}} \quad , \tag{58}$$

we see that, in the limit $z \to 0$, $r_{\max} \to 0$ as well. Further, since the height of the peak at $r_{\max}$,

$$D_{\max} = D(r_{\max}, z) = D(\frac{z}{\sqrt{2}}, z) = \frac{2}{3\sqrt{3}}\frac{1}{z} \quad , \tag{59}$$

is inversely proportional to z, in the limit $z \to 0$, $D_{\max}$ diverges at $r_{\max}$. Finally, since the area under $D(r_i, z)$ when integrated over z is also unity, and $D_{\max} \propto z$, it must be the case that the width of the distribution, $\Delta D(r_i, z)$, scales directly with z; hence, in the limit $z \to 0$, the peak also becomes infinitely sharp. Taken together, these facts imply that

$$\lim_{z \to 0} D(r_i, z) = \delta(r_i) \quad , \tag{60}$$

which makes evaluation of the integral in equation (32) trivial.

B. Analytic Expressions for B_r and B_z

Finding the magnetic field due to a prescribed distribution of "magnetic charge" amounts to solving a boundary value problem on a semi-infinite domain. If the field is assumed current free, i.e., $(\nabla \times \mathbf{B}) = 0$, then it can be described by a potential field, $\mathbf{B} = -\nabla\chi$. In such a case, the prescribed $\hat{\mathbf{z}}$-component of the vector field is a boundary condition on the potential. Modeling $\overline{B}_z$ in a sunspot distribution as Gaussian, one can solve for χ by assuming a Fourier inversion of $\overline{B}_z|_{z=0}$ exists:

$$\begin{aligned}
\chi(x,y,z,) &= \frac{1}{2\pi}\int_{-\infty}^{\infty} dk_x \int_{-\infty}^{\infty} dk_y \tilde{\chi}(k_x,k_y,z) e^{ik_x x} e^{ik_y y} \\
\Longrightarrow \nabla^2\chi &= \frac{1}{2\pi}\int_{-\infty}^{\infty} dk_x \int_{-\infty}^{\infty} dk_y [\frac{\partial^2\tilde{\chi}}{\partial z^2} - (k_x^2+k_y^2)\tilde{\chi}] e^{ik_x x} e^{ik_y y} = 0 \\
\Longrightarrow \tilde{\chi} &= C(k_x,k_y) e^{-\sqrt{k_x^2+k_y^2}z} \qquad (61) \\
\Longrightarrow \chi(x,y,z,) &= \frac{1}{2\pi}\int_{-\infty}^{\infty} dk_x \int_{-\infty}^{\infty} dk_y C(k_x,k_y) e^{-\sqrt{k_x^2+k_y^2}z} e^{ik_x x} e^{ik_y y}
\end{aligned}$$

$$\begin{aligned}
\sigma &= -\frac{1}{4\pi}[\frac{\partial\chi}{\partial n_+} - \frac{\partial\chi}{\partial n_-}] \Longrightarrow \qquad (62) \\
\left.\frac{\partial\chi}{\partial z}\right|_{z=0} &= -2\pi\sigma = -2\pi(q_0 N e^{-\frac{x^2}{2\delta^2}} e^{-\frac{y^2}{2\delta^2}}) = \overline{B}_z(x,y) \qquad (63) \\
-2\pi(q_0 N e^{-\frac{x^2}{2\delta^2}} e^{-\frac{y^2}{2\delta^2}}) &= -\frac{1}{2\pi}\int_{-\infty}^{\infty} dk_x \int_{-\infty}^{\infty} dk_y C(k_x,k_y)\sqrt{k_x^2+k_y^2} e^{ik_x x} e^{ik_y y}
\end{aligned}$$

Integration of both sides of this equation over the boundary surface gives:

$$q_0 N \underbrace{\int_{-\infty}^{\infty} dx\, e^{-\frac{x^2}{2\delta^2} - ik'_x x}}_{\sqrt{2\pi\delta^2} e^{\frac{-k'^2_x\delta^2}{2}}} \underbrace{\int_{-\infty}^{\infty} dy\, e^{-\frac{y^2}{2\delta^2} - ik'_y y}}_{\sqrt{2\pi\delta^2} e^{\frac{-k'^2_y\delta^2}{2}}} = \qquad (64)$$

$$\int_{-\infty}^{\infty}\int_{-\infty}^{\infty} dk_x\, dk_y\, C(k_x,k_y)\sqrt{k_x^2+k_y^2}\underbrace{\left(\frac{1}{2\pi}\int_{-\infty}^{\infty} dx\, e^{i(k_x-k_x')x}\right)}_{\delta(k_x-k_x')}\underbrace{\left(\frac{1}{2\pi}\int_{-\infty}^{\infty} dy\, e^{i(k_y-k_y')y}\right)}_{\delta(k_y-k_y')}$$

The integrations over Gaussians on the LHS were taken from Spiegel.

$$\begin{aligned}
\Longrightarrow C(k_x,k_y) &= (2\pi\delta^2)q_0N\frac{e^{\frac{-k_x^2\delta^2}{2}}e^{\frac{-k_y^2\delta^2}{2}}}{\sqrt{k_x^2+k_y^2}} \\
k_r^2\equiv k_x^2+k_y^2 \Longrightarrow C(k_r) &= (2\pi\delta^2)q_0N\frac{e^{\frac{-k_r^2\delta^2}{2}}}{k_r} \qquad (65)
\end{aligned}$$

$$\begin{aligned}
\Longrightarrow \chi(x,y,z) &= \frac{1}{2\pi}\int_0^{2\pi} d\phi'\int_0^{\infty} dk_r k_r(2\pi\delta^2)q_0N\frac{e^{\frac{-k_r^2\delta^2}{2}}}{k_r}e^{i\vec{k_r}\cdot\vec{r}}e^{-k_rz} \\
&= \delta^2q_0N\int_0^{\infty} dk_r e^{\frac{-k_r^2\delta^2}{2}}e^{-k_rz}\int_0^{2\pi} d\phi' e^{ik_rr\cos\phi'}
\end{aligned}$$

Rewriting the angular integral in two parts, one on $[0,\pi]$ and the other on $[\pi,2\pi]$ yields:

$$\int_0^{2\pi} d\phi' e^{ik_rr\cos\phi'} = \int_0^{\pi} d\phi' e^{ik_rr\cos\phi'} + \int_{\pi}^{2\pi} d\phi' e^{ik_rr\cos\phi'} \qquad (66)$$

Consider the change of variables $\phi' \longrightarrow \pi+\tilde{\phi}$: if $\phi'=\pi$, then $\tilde{\phi}=0$; and if $\phi'=2\pi$, then $\tilde{\phi}=\pi$; and $d\phi'=d\tilde{\phi}$. Now $\cos(\tilde{\phi}+\pi)=\cos(\tilde{\phi})\cos(\pi)+\sin(\tilde{\phi})\sin(\pi)=-\cos(\tilde{\phi})$, so the two integrals can be combined, using $2\cos(w)=e^{iw}+e^{-iw}$, to give:

$$\int_0^{2\pi} d\phi' e^{ik_rr\cos\phi'} = 2\int_0^{\pi} d\phi'\cos(k_rr\cos(\phi')) \qquad (67)$$

Gradshteyn & Ryzhik, # 8.411.5 is (cf., 8.411.7):

$$\begin{aligned}
\int_0^{\pi} d\phi'\cos(k_rr\cos(\phi')) &= \pi J_0(k_rr) \\
\int_0^{2\pi} d\phi' e^{ik_rr\cos\phi'} &= 2\pi J_0(k_rr) \Longrightarrow \\
\chi(x,y,z) &= \delta^2q_0N\int_0^{\infty} dk_r e^{\frac{-k_r^2\delta^2}{2}}e^{-k_rz}(2\pi J_0(k_rr)) \qquad (68)
\end{aligned}$$

Unfortunately, this integral is analytically intractable. Luckily, **B**, not χ, is the physically interesting quantity, and we can proceed by considering components of the former.

$$\mathbf{B} = -\nabla\chi = -\frac{\partial\chi}{\partial r}\hat{\mathbf{r}} - \frac{\partial\chi}{\partial z}\hat{\mathbf{z}} \Longrightarrow$$

$$B_r = -2\pi\delta^2 q_0 N \int_0^\infty dk_r\, k_r\, e^{\frac{-k_r^2\delta^2}{2}} J_0'(k_r r) e^{-k_r z} \tag{69}$$

$$B_z = -2\pi\delta^2 q_0 N \int_0^\infty dk_r\, (-k_r)\, e^{\frac{-k_r^2\delta^2}{2}} J_0(k_r r) e^{-k_r z} \tag{70}$$

The $\hat{\mathbf{r}}$ integral, at $z = 0$, is, after employing the well-known relation $J_0'(k_r r) = -J_1(k_r r)$:

$$B_r\Big|_{r=0} = 2\pi\delta^2 q_0 N \int_0^\infty dk_r\, k_r\, e^{\frac{-k_r^2\delta^2}{2}} J_1(k_r r) \tag{71}$$

Gradshteyn & Ryzhik, p. 738, # 6.631.7, is just this integral, with $x = k_r$, $\nu = 1$, $\alpha = \frac{\delta^2}{2}$, and $\beta = r$:

$$\int_0^\infty dx\, x\, e^{-\alpha x^2} J_\nu(\beta x) = \frac{\sqrt{\pi}\beta}{8\alpha^{\frac{3}{2}}} \exp(\frac{-\beta^2}{8\alpha}) \Big[I_{\frac{\nu}{2}-\frac{1}{2}}(\frac{\beta^2}{8\alpha}) - I_{\frac{\nu}{2}+\frac{1}{2}}(\frac{\beta^2}{8\alpha}) \Big]$$

$$\Longrightarrow B_r\Big|_{r=0} = 2\pi\delta^2 q_0 N \int_0^\infty dk_r\, k_r\, e^{\frac{-k_r^2\delta^2}{2}} J_1(k_r r)$$

$$= 2\pi\delta^2 q_0 N \frac{\sqrt{\pi} r}{8\frac{\delta^2}{2}^{\frac{3}{2}}} \exp(\frac{-r^2}{8\frac{\delta^2}{2}}) \Big[I_0(\frac{r^2}{8\frac{\delta^2}{2}}) - I_1(\frac{r^2}{8\frac{\delta^2}{2}}) \Big]$$

$$= \sqrt{\frac{\pi^3}{2}} \frac{q_0 N r}{\delta} \exp(\frac{-r^2}{4\delta^2}) \Big[I_0(\frac{r^2}{4\delta^2}) - I_1(\frac{r^2}{4\delta^2}) \Big] \tag{72}$$

The $\hat{\mathbf{z}}$ integral, also at $z = 0$, is

$$B_z\Big|_{z=0} = (-2\pi\delta^2 q_0 N) \int_0^\infty dk_r\, (-k_r)\, e^{\frac{-k_r^2\delta^2}{2}} J_0(k_r r) \tag{73}$$

But this is just the same integral applied in the radial case, but with $\nu = 0$, instead of $\nu = 1$. Consequently, its solution is simply

$$B_z\Big|_{z=0} = \sqrt{\frac{\pi^3}{2}}\frac{q_0 N r}{\delta} e^{\frac{-r^2}{4\delta^2}}\left[I_{0-\frac{1}{2}}(\frac{r^2}{4\delta^2}) - I_{0+\frac{1}{2}}(\frac{r^2}{4\delta^2})\right] \tag{74}$$

Spiegel, p.140, tells us

$$\begin{aligned} I_{-\frac{1}{2}}(\frac{r^2}{4\delta^2}) &= \sqrt{\frac{2}{\pi(\frac{r^2}{4\delta^2})}}\cosh(\frac{r^2}{4\delta^2}) \\ &= \sqrt{\frac{2}{\pi(\frac{r^2}{4\delta^2})}}\frac{(e^{\frac{r^2}{4\delta^2}} + e^{-\frac{r^2}{4\delta^2}})}{2} \end{aligned}$$

and

$$\begin{aligned} I_{\frac{1}{2}}(\frac{r^2}{4\delta^2}) &= \sqrt{\frac{2}{\pi(\frac{r^2}{4\delta^2})}}\sinh(\frac{r^2}{4\delta^2}) \\ &= \sqrt{\frac{2}{\pi(\frac{r^2}{4\delta^2})}}\frac{(e^{\frac{r^2}{4\delta^2}} - e^{-\frac{r^2}{4\delta^2}})}{2} \end{aligned}$$

Now $(\cosh(x) - \sinh(x)) = \frac{1}{2}(e^x + e^{-x} - e^x + e^{-x}) = e^{-x}$, so the full solution for B_z is

$$B_z\Big|_{z=0} = \sqrt{\frac{\pi^3}{2}}\frac{q_0 N r}{\delta} e^{\frac{-r^2}{4\delta^2}} \sqrt{\frac{2}{\pi(\frac{r^2}{4\delta^2})}} e^{\frac{-r^2}{4\delta^2}} = 2\pi q_0 N e^{\frac{-r^2}{2\delta^2}} \quad , \tag{75}$$

as expected.

C. B_r Far from the Origin

From Abramowitz & Stegun, p. 377, with ν fixed, $|\, z \,|$ large, and $\mu \equiv 4\nu^2$,

$$I_\nu(z) \sim \frac{e^z}{\sqrt{2\pi z}}\left\{1 - \frac{\mu-1}{8z} + \frac{(\mu-1)(\mu-9)}{(2!)(8z)^2} - \frac{(\mu-1)(\mu-9)(\mu-25)}{(3!)(8z)^3} + \ldots\right\}$$

Setting $z = w^2$, where $w \propto r$, gives:

$$\Longrightarrow I_0(w^2) = \frac{e^{w^2}}{\sqrt{2\pi w^2}}\left\{1 + \frac{1}{8w^2} + \frac{9}{2(8w^2)^2} - \ldots\right\} \tag{76}$$

and

$$\Longrightarrow I_1(w^2) = \frac{e^{w^2}}{\sqrt{2\pi w^2}}\left\{1 - \frac{3}{8w^2} - \frac{15}{2(8w^2)^2} - \ldots\right\} \tag{77}$$

$$\Longrightarrow B_r \propto we^{-w^2}\Big[I_0(w^2) - I_1(w^2)\Big] \tag{78}$$

$$= \frac{1}{\sqrt{2\pi}}\left\{1 + \frac{1}{8w^2} + \frac{9}{2(8w^2)^2} + \ldots - 1 + \frac{3}{8w^2} + \frac{15}{2(8w^2)^2} - \ldots\right\}$$

$$= \frac{1}{\sqrt{2\pi}}\left\{\frac{1}{2w^2} + \frac{3}{16w^4} - \ldots\right\} \tag{79}$$

So, as expected, $B_r|_{r \gg \delta} \propto \frac{1}{r^2}$.

References Cited

Abramowitz, M., & Stegun, I. A. 1964, Handbook of Mathematical Functions (New York: Dover)

Baum, P. J., & Bratenahl, A. 1980, Solar Phys., 67, 245

Caligari, P., Moreno-Insertis, F., & Schüssler, M. 1995, ApJ, 441, 886

Canfield, R. C., & Metcalf, T. R. 1987, ApJ, 321, 586

Cowley, S. W. H. 1973, Radio Sci., 8, 903

Démoulin, P., Hénoux, J., & Mandrini, C. 1994, A&A, 285, 1023

D'Silva, S., & Choudhuri, A. R. 1993, A&A, 272, 621

Fan, Y., Fisher, G. H., & McClymont, A. N. 1994, ApJ, 436, 907

Gabriel, A. H. 1976, Phil. Trans. R. Soc. Lond., A281, 339

Gary, D. E., Hartl, M. D., & Shimizu, T. 1997, ApJ, 477, 958

Gold, T., & Hoyle, F. 1960, MNRAS, 120, 89

Gorbachev, V. S., & Somov, B. V. 1988, Solar Phys., 117, 77

Gradshteyn, I. S., & Ryzhik, I. M. 1965, Table of Integrals, Series, and Products (San Diego: Academic Press)

Hood, A. W., & Priest, E. R. 1979, Solar Phys., 64, 303

Lau, Y.-T. 1993, Solar Phys., 148, 301

Leighton, R. B. 1964, ApJ, 140, 1547

Lin, R. P., Schwartz, R. A., Kane, S. R., Pelling, R. M., & Hurley, K. C. 1984, ApJ, 283, 421

Longcope, D. W. 1996, Solar Phys., 169, 91

Longcope, D. W. 1998, ApJ, Submitted

Longcope, D. W., & Cowley, S. C. 1996, Phys. Plasmas, 3, 2885

Low, B. C. 1977, ApJ, 212, 234

Moffatt, H. K. 1978, Magnetic Field Generation in Electrically Conducting Fluids (Cambridge: Cambridge University Press)

Osterbrock, D. E. 1961, ApJ, 134, 347

Parker, E. N. 1955, ApJ, 121, 491

Parker, E. N. 1988, ApJ, 330, 474

Parnell, C. E., Priest, E. R., & Golub, L. 1994, Solar Phys., 151, 57

Porter, L. J., & Klimchuk, J. A. 1995, ApJ, 454, 499

Porter, L. J., Klimchuk, J. A., & Sturrock, P. A. 1994, ApJ, 435, 482

Priest, E. R. 1982, Solar Magnetohydrodynamics, Vol. 21 (Boston: D. Reidel)

Priest, E. R., & Forbes, T. G. 1989, Solar Phys., 119, 211

Shimizu, T. 1995, Publ. Astron. Soc. Japan, 47, 251

Shimizu, T., Tsuneta, S., Acton, L. W., Lemen, J. R., Ogawara, Y., & Uchida, Y. 1994, ApJ, 422, 906

Shimizu, T., Tsuneta, S., Acton, L. W., Lemen, J. R., & Uchida, Y. 1992, Proc. Astron. Soc. Japan, 44, L147

Somov, B. V. 1992, Physical Processes in Solar Flares (Kluwer)

Spiegel, M. R. 1968, Mathematical Handbook of Formulas and Tables (New York: McGraw-Hill)

Sweet, P. A. 1958, in Electromagnetic Phenomena in Cosmical Physics, ed. B. Lehnert (Cambridge, U.K.: Cambridge University Press), 123

Van Hoven, G., et al. 1980, in Solar Flares. A monograph from Skylab Solar Workshop II, ed. P. A. Sturrock (Colorado Associated University Press), 17

Yeh, T. 1976, JGR, 81, 2140

MONTANA STATE UNIVERSITY LIBRARIES
3 1762 10274501 3